Journal of Computational Physics 524 (2025) 113737

Contents lists available at ScienceDirect

Journal of Computational Physics

journal homepage: www.elsevier.com/locate/jcp

Fully discrete finite element method with full decoupling structure and second-order temporal accuracy for a flow-coupled dendritic solidification phase-field model

Jun Zhang [a], Kejia Pan [b], Xiaofeng Yang [c,*]

[a] Computational Mathematics Research Center, Guizhou University of Finance and Economics, Guiyang, Guizhou 550025, China
[b] School of Mathematics and Statistics, HNP-LAMA, Central South University, Changsha 410083, China
[c] Department of Mathematics, University of South Carolina, Columbia, SC 29208, USA

ARTICLE INFO

Keywords:
Phase-field
Decoupled
Second-order
Projection method
Dendritic
Navier-Stokes

ABSTRACT

The development of effective numerical methods for simulating the dendritic solidification process using the flow-coupled, melt-convective phase-field model has consistently encountered challenges due to the model's complex nonlinear and coupled structures. The major concern of algorithm design is to ensure a numerical scheme that achieves second-order accuracy in time, maintains linearity and attains a fully decoupled structure. All these objectives are accomplished within the framework of guaranteed unconditional energy stability, which is addressed by the fully discrete finite element scheme proposed in this paper. The developed scheme uses the modified projection-type method to deal with the "weighted" Navier-Stokes equations, and the complete decoupling feature is achieved by using the explicit-SAV (Scalar Auxiliary Variable) method, which also helps to linearize the nonlinear potentials. The scheme simplifies its procedure by only requiring the solution of several completely decoupled and linear elliptic equations at every time step, which facilitates its easy implementation. The solvability and energy stability are further rigorously validated. Comprehensive details of the procedural steps for implementation are also provided, accompanied by plenty of numerical tests conducted in both 2D and 3D, serving to numerically ascertain the accuracy and robustness of the scheme.

1. Introduction

When materials crystallize or solidify, often due to changes in temperature or concentration, they usually form complex, branch-like patterns known as dendritic structures, similar to those seen in snowflakes or frost on windows. The phase-field method excels in modeling complex interfaces in science and engineering due to its simplicity and flexibility, making it a preferred choice for modeling dendritic solidification processes. This approach's usefulness in portraying the evolution of dendritic structures has been demonstrated in seminal works by Kobayashi [14] and further explored in numerous subsequent studies in [10–13,15,16,40]. Utilizing the phase-field approach for dendritic solidification modeling entails the introduction of a scalar phase-field variable, which serves to distinguish between solid and liquid states, forming the basis for a detailed free energy model of the system. The system's total free energy is commonly postulated to comprise three fundamental components: configurational entropy, which dictates spatial

* Corresponding author.
E-mail addresses: jzhang@mail.gufe.edu.cn (J. Zhang), kejiapan@csu.edu.cn (K. Pan), xfyang@math.sc.edu (X. Yang).

https://doi.org/10.1016/j.jcp.2025.113737
Received 3 June 2024; Received in revised form 1 January 2025; Accepted 8 January 2025

Available online 14 January 2025

anisotropy; a double-well nonlinear potential, essential for delineating the distinct phases; and a thermal potential, indicative of temperature variations. The model's governing dynamics are formulated by invoking gradient flow methodologies, similar to the Allen-Cahn and Cahn-Hilliard frameworks, applied to the system's total free energy and enthalpy [12,14].

Typically, the most basic phase-field models for dendritic growth incorporate a duo of coupled equations: one addressing the evolution of the phase-field variable to chart dendritic interfaces' growth, and the other managing the thermal field to monitor temperature evolution [12,14], with their interaction representing the transfer of latent heat. Such foundational models typically sideline the role of external fluid dynamics in the solidification process, focusing predominantly on latent heat's impact. Nevertheless, in scenarios where external fluid flow velocities become significant, it's imperative to enhance these models to account for the influence of ambient fluid dynamics on the liquid-solid phase transitions. Beckermann et al. pioneered this extension, integrating the impact of external fluid dynamics into the modeling of phase transitions between liquid and solid states [2,25], in which, a key innovation is the use of a specific "weight" function, that realizes the restriction of the effects of temperature convection, fluid momentum, and mass conservation strictly to the liquid phase, thus refining the model by eliminating the fluid dynamics within the solid phase and maintaining the Navier-Stokes equations' validity in the liquid domain.

While Beckermann et al.'s flow-coupled phase-field dendritic model in [2,25] has received extensive attention, it's imperative to acknowledge that the model, in its original form, does not comply with the energy law, a critical aspect for ensuring the physical validity of simulations. In response to this limitation, recent efforts have been undertaken to amend the model, aligning it with the energy dissipation principle, see the authors' work in [4]. However, the development of numerical algorithms for both the original and amended versions of these flow-coupled dendritic models remains limited, and the bulk of existing numerical research [4,10,11,15,16,40] tends to concentrate more on exploring the outcomes achievable through fine-tuning the models' parameters, rather than on the development of numerical techniques tailored to these models' unique characteristics. This gap in developing numerical algorithms can be attributed to the models' inherent complexity, which poses formidable challenges in meeting high standards like linearity, second-order temporal accuracy, decoupled structures, and unconditional energy stability. Fulfilling all these criteria gives rise to what we identify as "desired" schemes in this paper, highlighting the significant hurdles in crafting such algorithms for this particular flow-coupled phase-field dendrite solidification model.

So, what specifically makes it so challenging to develop a "desired" type scheme for this model? The difficulty primarily stems from a significant number of coupled nonlinear terms, including the latent heat transfer term that binds the phase-field variable with the temperature, the weight function combined with many complex coupling terms in the modified Navier-Stokes equations, as well as the advective term in the heat equation. To date, there are only two numerical schemes with energy stability for this model, both of which were developed in the authors' prior work [4,39], one features a coupled framework, while the other employs a decoupled approach. Moreover, both schemes in [4,39] are only first-order accurate in time and require solving variable-coefficient systems, which poses a drawback on computational efficiency and accuracy. Hence, devising a scheme that encompasses all the desired features—second-order temporal accuracy, a linear and fully decoupled structure, along with unconditional energy stability during time marching—stands as a significant challenge that remains unresolved.

In this article, we aim to bridge the gap between a well-established model and its less-developed numerical methods by devising a novel scheme that encapsulates the "desired" characteristics for effectively solving the phase-field dendritic solidification model when it is coupled with the flow field. This scheme not only achieves second-order temporal accuracy and unconditional energy stability but also facilitates decoupled computations, which allows for the independent computation of every unknown variable at every time step, significantly boosting computational efficiency. The approach to constructing the numerical scheme integrates a variety of proven effective techniques. The finite element method is utilized for spatial discretization. The explicit-Scalar Auxiliary Variable (SAV) [5,17,18,34] method is developed for time discretization, which, when combined with the Zero-Energy-Contribution (ZEC) approach [29–32] alongside the projection-type method, enables us to achieve the complete decoupling. The core of our developed methodology involves introducing several nonlocal auxiliary variables and formulating their respective ordinary differential equations (ODEs) to transform the system into an equivalent but more "algorithm-friendly" version. By applying a specific linear splitting technique through the nonlocal variables, we can break down the discrete equations into several linear and independent elliptic sub-equations at each time step, leading to an effective and efficient computational strategy. According to the author's awareness, no existing schemes have been able to encompass all these desired properties within a single scheme.

The structure of the remainder of this paper is as follows: in Section 2, we introduce the melt-convective, flow-coupled dendritic solidification phase-field model, including the derivation of its energy law. We develop the numerical scheme in its fully discrete version using the finite element method in Section 3. We also show in detail how to implement the scheme in a fully decoupled manner and rigorously establish its solvability and unconditional energy stability. In Section 4, we apply the proposed scheme to simulate the 2D and 3D flow-driven dendritic crystal growth. Some concluding remarks are provided in Section 5.

2. The governing system

The phase-field model for dendritic solidification, which integrates flow-coupled melt convection, was first introduced in [2,25] and subsequently modified in the authors' previous studies [4,39] to ensure compliance with the law of energy dissipation. Given the close similarity between the two versions, we will primarily discuss the modified model, providing details of the original formulation in the Remark 2.1.

We consider a domain $\Omega \in \mathbb{R}^d$ with $d = 2, 3$ characterized as smooth, open, bounded, and connected. The domain is composed of two distinct phases, solid and liquid, differentiated by the so-called phase-field function $\phi(\boldsymbol{x}, t) \in \mathbb{R}, \boldsymbol{x} \in \Omega$, which is defined as:

$$\phi(\boldsymbol{x},t)=\begin{cases}1 & \text{solid},\\ -1 & \text{liquid},\end{cases} \tag{2.1}$$

which helps identify each phase. To address the discontinuity in ϕ, it is assumed that there is a thin, smooth transition region at the interface, characterized by a width on the order of $O(\epsilon)$. Moreover, we define another scalar function $T(\mathbf{x},t), \boldsymbol{x}\in\Omega$ to denote the temperature field across the domain, which is expressed in the dimensionless form.

Hence, the slightly-refined model for flow-coupled anisotropic phase-field dendritic solidification, which adheres to the modified energy law, as developed in [4,39] (with the original formulation presented in [2,25]), is described as follows.

$$\frac{1-\phi}{2}\left(\frac{1-\phi}{2}\mathbf{u}\right)_t+\frac{1-\phi}{2}(\mathbf{u}\cdot\nabla)\mathbf{u}-\nu\nabla\cdot(\frac{1-\phi}{2}\nabla\mathbf{u})+\frac{1-\phi}{2}\nabla P=-\nu\xi q(\phi)\mathbf{u}, \tag{2.2}$$

$$\nabla\cdot(\frac{1-\phi}{2}\mathbf{u})=0, \tag{2.3}$$

$$\tau\phi_t=\nabla\cdot(\kappa^2(\nabla\phi)\nabla\phi+\kappa(\nabla\phi)|\nabla\phi|^2\boldsymbol{\zeta}(\phi))-\frac{1}{\epsilon^2}f(\phi)-\frac{\lambda}{\epsilon}p(\phi)T, \tag{2.4}$$

$$T_t+(\frac{1-\phi}{2})\mathbf{u}\cdot\nabla T=D\Delta T+Kp(\phi)\phi_t. \tag{2.5}$$

In the above context, $\mathbf{u}$ represents the average fluid velocity field, P denotes the pressure, ν indicates the kinematic viscosity, ξ defines the scaled characteristic interfacial width, $q(\phi)=(1-\phi^2)(1+\phi)$, D represents the diffusion rate of the temperature, λ and K are associated with the "latent heat" (cf. [14]), the function $f(\phi)=F'(\phi)$ with $F(\phi)=\frac{(\phi^2-1)^2}{4}$, describes a double-well type potential, $\kappa(\nabla\phi)$ is the anisotropic coefficient, τ represents a positive mobility parameter and is set to be a constant (cf. [13,26]), $p(\phi)=(1-\phi^2)^2$ specifies that the transfer of latent heat is confined to the liquid-solid interface (cf. [12]), and the term $\boldsymbol{\zeta}(\phi)$ corresponds to the variational derivative of $\kappa(\nabla\phi)$. The last term $-\nu\xi q(\phi)\mathbf{u}$, within the momentum equation (2.2) contributes additional viscous dissipative stress, acting as a dispersed momentum sink in the diffuse interface region (cf. [2,25]). Notably, this term is absent in the homogeneous solid and liquid regions, exclusively affecting the interface between these two phases.

Remark 2.1. In the original model developed by Beckermann et al. in [2], the momentum equation is given as

$$\left(\frac{1-\phi}{2}\mathbf{u}\right)_t+\frac{1-\phi}{2}(\mathbf{u}\cdot\nabla)\mathbf{u}-\nu\Delta(\frac{1-\phi}{2}\mathbf{u})+\frac{1-\phi}{2}\nabla P=-\nu\xi q(\phi)\mathbf{u}. \tag{2.6}$$

However, the formulation (2.6) does not satisfy the energy dissipation law, a fact that becomes evident when performing an L^2-inner product of (2.6) with the velocity field $\mathbf{u}$. Thus, in our previous work in [4,39], we introduced a minor yet crucial modification to the momentum equation, see (2.2). This amendment ensures compliance with energy dissipation laws and remarkably replicates the dendritic morphologies observed in Beckermann's original model, see the details in [4,39].

Generally, the definition of $\kappa(\nabla\phi)$ reads as

$$\kappa(\nabla\phi)=1+\epsilon_4\cos(m\Theta), \tag{2.7}$$

where m represents the count of anisotropy folds, $0\le\epsilon_4\le 1$ is a parameter indicating the magnitude of anisotropy, and $\Theta=\arctan(\frac{\phi_y}{\phi_x})$. We also have $\kappa(\nabla\phi)\ge 1-\epsilon_4$.

When $m=4$ (four-fold anisotropy), the following format of $\kappa(\nabla\phi)$ is also frequently adopted:

$$\begin{cases}\kappa(\nabla\phi)=(1-3\epsilon_4)\Big(1+\dfrac{4\epsilon_4}{1-3\epsilon_4}\dfrac{\phi_x^4+\phi_y^4}{|\nabla\phi|^4}\Big) \text{ for 2D case;}\\ \kappa(\nabla\phi)=(1-3\epsilon_4)\Big(1+\dfrac{4\epsilon_4}{1-3\epsilon_4}\dfrac{\phi_x^4+\phi_y^4+\phi_z^4}{|\nabla\phi|^4}\Big) \text{ for 3D case.}\end{cases} \tag{2.8}$$

For $m=4$, by taking the variational derivative of $\kappa(\nabla\phi)$, we derive $\boldsymbol{\zeta}(\phi)$ as

$$\begin{cases}\boldsymbol{\zeta}(\phi)=\dfrac{\delta\kappa(\nabla\phi)}{\delta\phi}=4\epsilon_4\dfrac{4}{|\nabla\phi|^6}\Big(\phi_x(\phi_x^2\phi_y^2-\phi_y^4),\ \phi_y(\phi_x^2\phi_y^2-\phi_x^4)\Big) \text{ for 2D case;}\\ \boldsymbol{\zeta}(\phi)=\dfrac{\delta\kappa(\nabla\phi)}{\delta\phi}=4\epsilon_4\dfrac{4}{|\nabla\phi|^6}\Big(\phi_x(\phi_x^2\phi_y^2+\phi_x^2\phi_z^2-\phi_y^4-\phi_z^4),\\ \qquad\phi_y(\phi_y^2\phi_z^2+\phi_x^2\phi_y^2-\phi_x^4-\phi_z^4),\ \phi_z(\phi_x^2\phi_z^2+\phi_y^2\phi_z^2-\phi_x^4-\phi_y^4)\Big) \text{ for 3D case.}\end{cases} \tag{2.9}$$

Without losing generality, the Dirichlet-type boundary conditions are used for $\mathbf{u}$, and no-flux boundary conditions are used for ϕ and T, specified as follows:

$$\mathbf{u}|_{\partial\Omega}=\mathbf{0},\partial_{\mathbf{n}}\phi|_{\partial\Omega}=\partial_{\mathbf{n}}T|_{\partial\Omega}=0, \tag{2.10}$$

where $\mathbf{n}$ is the normal vector pointing outward from the domain boundary. Periodic-type boundary conditions are commonly applied to all variables when simulating the model without incorporating the flow field, see [4,10,11,15,16,40]. Additionally, the initial conditions for the system (2.2)-(2.5) are specified as follows:

$$\mathbf{u}|_{(t=0)} = \mathbf{u}_0, P|_{(t=0)} = P_0, \phi|_{(t=0)} = \phi_0, T|_{(t=0)} = T_0. \tag{2.11}$$

The system (2.2)-(2.5) represents a binary mixture where phase transitions occur between the liquid and solid phases. For the no-flow case (by setting $\mathbf{u} = 0$), the derivation of the PDE system (2.4)-(2.5) utilizes the variational formulation (VF) method, as extensively described in [12]. This VF method can be viewed as a hybrid variational approach. It incorporates Allen-Cahn dynamics—an L^2-gradient flow mechanism—to formulate the ϕ-equation from the system's total free energy $E(\mathbf{u}, \phi, T)$. Meanwhile, the temperature equation for T employs the H^{-1}-gradient flow, often referred to as Cahn-Hilliard dynamics, which is applied to the enthalpy in the dimensionless form, denoted as $T - \frac{\tilde{P}(\phi)}{2}$, where $\tilde{P}'(\phi) = p(\phi)$. These derivations are extensively detailed in [12]. Meanwhile, the parameters used in (2.4)-(2.5) are essentially a re-scaling of those used in [12].

When incorporating the flow field $\mathbf{u}$, it becomes essential to restrict the fluid momentum equation to the liquid phase exclusively. The model (2.2)-(2.5) adopts a straightforward approach, a weight factor $\frac{1-\phi}{2}$, which is used to enforce a limitation, ensuring that the momentum of the fluid is considered only in the liquid phase. Specifically, inside the solid phase with ϕ equal to 1, both the momentum equation (2.2) and the incompressibility condition (2.3) become nullified. Within the liquid phase with ϕ equal to -1, (2.2)-(2.3) reduce to the classical Navier-Stokes equations. This methodology was initially introduced in [2] and has since been widely adopted in phase-field modeling of complex systems, such as the binary mixture of liquid crystal and viscous fluid, see [22,36,37].

We now show that the model for dendritic growth, (2.2)-(2.5), admits the energy dissipative law, which is achieved by conducting a standard energy estimate process, described as follows. Before presenting the proof, we introduce several notations that will be consistently used in this article. The L^2-inner product of any two functions $\phi(\boldsymbol{x})$ and $\psi(\boldsymbol{x})$ over Ω is defined as $(\phi, \psi) = \int_\Omega \phi(\boldsymbol{x})\psi(\boldsymbol{x})d\boldsymbol{x}$. Additionally, the L^2-norm of $\phi(\boldsymbol{x})$ is given by $\|\phi\| = (\phi, \phi)^{\frac{1}{2}}$.

Lemma 2.1. *The system* (2.2)-(2.5) *satisfies the following energy law:*

$$\frac{d}{dt}E(\mathbf{u}, \phi, T) = -\tau\|\phi_t\|^2 - \frac{\lambda D}{\epsilon K}\|\nabla T\|^2 - \nu(\frac{1-\phi}{2}\nabla\mathbf{u}, \nabla\mathbf{u}) - \nu\xi(q(\phi)\mathbf{u}, \mathbf{u}), \tag{2.12}$$

where

$$E(\mathbf{u}, \phi, T) = \int_\Omega \left(\frac{1}{2}\left|\frac{1-\phi}{2}\mathbf{u}\right|^2 + \frac{1}{2}|\kappa(\nabla\phi)\nabla\phi|^2 + \frac{1}{4\epsilon^2}F(\phi) + \frac{\lambda}{2\epsilon K}|T|^2\right)d\boldsymbol{x}. \tag{2.13}$$

Proof. First, by taking the L^2-inner product of (2.2) with $\mathbf{u}$, and using the divergence-free condition given in (2.3) and integration by parts, we get

$$\frac{d}{dt}\int_\Omega \left(\frac{1}{2}\left|\frac{1-\phi}{2}\mathbf{u}\right|^2\right)d\boldsymbol{x} = \underbrace{-(\frac{1-\phi}{2}(\mathbf{u}\cdot\nabla)\mathbf{u}, \mathbf{u})}_{\text{I}} - \nu(\frac{1-\phi}{2}\nabla\mathbf{u}, \nabla\mathbf{u}) - \nu\xi(q(\phi)\mathbf{u}, \mathbf{u}). \tag{2.14}$$

Second, by performing the L^2-inner product on (2.4) with ϕ_t, and applying integration by parts, we derive

$$\tau\|\phi_t\|^2 + \frac{d}{dt}\int_\Omega \left(\frac{1}{2}|\kappa(\nabla\phi)\nabla\phi|^2 + \frac{1}{4\epsilon^2}F(\phi)\right)d\boldsymbol{x} = \underbrace{-\frac{\lambda}{\epsilon}(p(\phi)T, \phi_t)}_{\text{II}}. \tag{2.15}$$

Third, by computing the L^2-inner product of (2.5) with $\frac{\lambda}{\epsilon K}T$ and using integration by parts, we derive

$$\frac{d}{dt}\int_\Omega \frac{\lambda}{2\epsilon K}|T|^2 d\boldsymbol{x} + \frac{\lambda D}{\epsilon K}\|\nabla T\|^2 = \underbrace{\frac{\lambda}{\epsilon}(p(\phi)\phi_t, T)}_{\text{III}} \underbrace{-\frac{\lambda}{\epsilon K}\left(\frac{1-\phi}{2}\mathbf{u}\cdot\nabla T, T\right)}_{\text{IV}}. \tag{2.16}$$

Combining the three obtained equalities (2.14)-(2.16), and noting that the term I vanishes due to the divergence-free condition (2.3) and the boundary condition $\frac{1-\phi}{2}\mathbf{u}\cdot\mathbf{n}|_{\partial\Omega} = 0$, terms II and III cancel each other out, and the term IV also vanishes by the same reasoning as term I, we arrive at (2.12). □

A few remarks are given as follows to clarify the details related to the energy law (2.12) within the model (2.2)-(2.5).

Remark 2.2. For a closed thermodynamical system, it's established that energy dissipation must occur. However, the final two terms on the right side of (2.12) may be non-negative, which casts doubt on the certainty of energy dissipation. Thus, the energy law as presented in (2.12) holds "physical" merit primarily under ideal conditions where the variable ϕ consistently stays within the $[-1, 1]$

range, facilitating the diminution of total free energy. Yet, from a mathematical perspective, proving that the solution to this PDE system adheres to the maximum principle poses a significant challenge.

Similarly, designing a numerical scheme that guarantees the numerical solution for ϕ remains bounded within $[-1, 1]$, thereby adhering to the discrete maximum principle, presents an equally daunting challenge. Therefore, rather than employing advanced techniques to strictly control the range of ϕ in the numerical solution, the "clamping" method is utilized in the design of the discrete numerical scheme to address the issue of potential non-dissipative energy. This approach involves constraining ϕ within a slightly narrower range of $[-1+\varepsilon, 1-\varepsilon]$, with a small positive control parameter $\varepsilon \ll 1$, as detailed in (3.35), effectively sidestepping the complexities associated with ensuring maximum bounds.

Remark 2.3. The system exhibits a notable characteristic termed the "zero-energy-contribution" property, as demonstrated in Lemma 2.1. It is found that the application of both the divergence-free condition and boundary condition results in the elimination of terms I and IV, while terms II and III are observed to counteract each other. This leads to the insight that, upon the execution of specific inner products, these terms do not affect the energy law, making it fitting to categorize them under the "zero-energy-contribution" label.

The implementation of this characteristic in the design of algorithms for other coupled models is explored in the authors' previous studies, cf. [31,33,35]. However, adapting this strategy to the dendritic model discussed in this paper encounters significant obstacles, particularly due to the unique nonlinear terms and their coupling mechanisms between variables. Therefore, despite the established methodology, the distinct complexities inherent to this specific model complicate the direct application of this approach.

3. Numerical scheme

Now, we are ready to design an efficient fully discrete scheme using the finite element method for solving the model of flow-coupled, melt-convective dendritic solidification. We expect that the scheme can possess several "desired" attributes: unconditional energy stability, linearity, second-order temporal accuracy, and fully decoupled structure. Achieving all these favorable characteristics within a single algorithm is far from trivial, given the inherent complexities of the model. These complexities include various elements such as the nonlinear and/or coupled terms related to $f(\phi)$, $\kappa(\nabla\phi)$, $p(\phi)$, and $\frac{1-\phi}{2}$, among others. Each of these factors contributes to the model's overall complexity and represents significant challenges in the development of robust and effective computational methodologies.

To develop the "desired" scheme, we start by recasting the PDE system into a version that is more amenable to algorithmic implementation, yet remains equivalent to the original formulation.

3.1. Reformulated system

We reconfigure the PDE system (2.2)-(2.5) by integrating several nonlocal type auxiliary variables into the framework. It's imperative to emphasize that this adjusted PDE system maintains its equivalence to the original equations, serving as the cornerstone of our methodology.

To begin, we introduce a new auxiliary variable of the nonlocal type, denoted by $U(t)$, aimed at converting the nonlinear portion of the energy potential into a quadratic form. The variable $U(t)$ is defined in the following manner:

$$U(t) = \sqrt{\int_\Omega \left(\frac{1}{2}(\kappa^2(\nabla\phi) - S_1)|\nabla\phi|^2 + \frac{1}{4\epsilon^2}(F(\phi) - 2S_2\phi^2)\right)d\boldsymbol{x} + B}, \tag{3.1}$$

where S_1 and S_2 are two predetermined positive constants with $0 < S_1 < (1-\epsilon_4)^2$. Since $F(\phi)$ is a quartic polynomial with a leading term that is positive, it ensures that, upon the extraction of a quadratic component related to S_2, this potential can consistently provide a lower bound. Furthermore, considering that $\kappa^2(\nabla\phi) \geq (1-\epsilon_4)^2$, the radicand in (3.1) is guaranteed to be bounded from below. To enhance positivity further, we incorporate the constant B into the radicand. Utilizing the auxiliary nonlocal variable $U(t)$, and transforming the nonlinear segment of the energy potential to be U^2, is known as the SAV method (cf. [20,24,28,38,39]).

Using the new variable U, we reformulate (2.4) into an equivalent form:

$$\begin{cases} \tau\phi_t - S_1\Delta\phi + \dfrac{S_2}{\epsilon^2}\phi = -HU - \dfrac{\lambda}{\epsilon}p(\phi)T, \\ U_t = \dfrac{1}{2}\displaystyle\int_\Omega H\phi_t d\boldsymbol{x}, \\ U|_{(t=0)} = U(\phi_0), \end{cases} \tag{3.2}$$

where

$$H(\phi) = \frac{-\nabla\cdot((\kappa^2(\nabla\phi) - S_1)\nabla\phi + \kappa(\nabla\phi)|\nabla\phi|^2\boldsymbol{\zeta}(\phi)) + \frac{1}{\epsilon^2}f(\phi) - \frac{S_2}{\epsilon^2}\phi}{\sqrt{\int_\Omega(\frac{1}{2}(\kappa^2(\nabla\phi) - S_1)|\nabla\phi|^2 + \frac{1}{4\epsilon^2}(F(\phi) - 2S_2\phi^2))d\boldsymbol{x} + B}}. \tag{3.3}$$

It is immediately apparent that there is an equivalence between (3.2) and (2.4). It is because integrating the second equation from (3.2) and considering the initial condition of $U|_{(t=0)}$ allows the complete restoration of the formulation in (2.4). This step highlights the inherent equivalence of the two expressions.

Next, we define another nonlocal auxiliary variable, $Q(t)$, and construct a particular ODE for its temporal evolution, which is expressed as follows:

$$\begin{cases} Q_t = \dfrac{\lambda}{\epsilon}(p(\phi)T, \phi_t) - \dfrac{\lambda}{\epsilon}(p(\phi)\phi_t, T) + (HU, \phi_t) - (H\phi_t, U) + \dfrac{\lambda}{\epsilon K}\left(\dfrac{1-\phi}{2}\mathbf{u}\cdot\nabla T, T\right), \\ Q|_{(t=0)} = 1. \end{cases} \tag{3.4}$$

The distinct feature of the above ODE lies in the fact that every term on the right-hand side of (3.4) is composed of L^2-inner product terms, and their sum is exactly zero, which is confirmed by the proof in Lemma 2.1, namely, $Q_t = 0$. Therefore, since $Q|_{(t=0)} = 1$, (3.4) directly leads to the solution $Q(t) = 1$.

Third, we introduce the third auxiliary variable, $R(t)$, also of the nonlocal type, and design a specific ODE for its time evolution, that is formulated as

$$\begin{cases} R_t = \left(\dfrac{1-\phi}{2}(\mathbf{u}\cdot\nabla)\mathbf{u}, \mathbf{u}\right), \\ R|_{(t=0)} = 1. \end{cases} \tag{3.5}$$

From the proof of Lemma 2.1, we can see that $R_t = 0$. Thus, using $R|_{(t=0)} = 1$, the solution of the ODE system (3.5) is also trivial, namely, $R(t) = 1$.

For the model described by equations (2.4)-(2.5), we utilize (3.2) to replace (2.4). Furthermore, the nonlocal variables Q and R, along with their respective ODEs, (3.4) and (3.5), are used to alter particular terms in the system. This comprehensive combination culminates in a revised system, detailed as follows:

$$\frac{1-\phi}{2}\left(\frac{1-\phi}{2}\mathbf{u}\right)_t + \underbrace{R\frac{1-\phi}{2}(\mathbf{u}\cdot\nabla)\mathbf{u}}_{\text{R-reform}} - \nu\nabla\cdot\left(\frac{1-\phi}{2}\nabla\mathbf{u}\right) + \frac{1-\phi}{2}\nabla P = -\nu\xi q(\phi)\mathbf{u}, \tag{3.6}$$

$$\nabla\cdot\left(\frac{1-\phi}{2}\mathbf{u}\right) = 0, \tag{3.7}$$

$$\tau\phi_t - S_1\Delta\phi + \frac{S_2}{\epsilon^2}\phi = \underbrace{-QHU}_{\text{Q-reform}} - \underbrace{\frac{\lambda}{\epsilon}Qp(\phi)T}_{\text{Q-reform}}, \tag{3.8}$$

$$T_t + \underbrace{Q\left(\frac{1-\phi}{2}\right)\mathbf{u}\cdot\nabla T}_{\text{Q-reform}} = D\Delta T + \underbrace{KQp(\phi)\phi_t}_{\text{Q-reform}}, \tag{3.9}$$

$$U_t = \underbrace{\frac{1}{2}Q\int_\Omega H\phi_t\, d\boldsymbol{x}}_{\text{Q-reform}}, \tag{3.10}$$

$$Q_t = \frac{\lambda}{\epsilon}(p(\phi)T, \phi_t) - \frac{\lambda}{\epsilon}(p(\phi)\phi_t, T) + (HU, \phi_t) - (H\phi_t, U) + \frac{\lambda}{\epsilon K}\left(\frac{1-\phi}{2}\mathbf{u}\cdot\nabla T, T\right), \tag{3.11}$$

$$R_t = \left(\frac{1-\phi}{2}(\mathbf{u}\cdot\nabla)\mathbf{u}, \mathbf{u}\right), \tag{3.12}$$

with the boundary conditions specified in (2.10) and the following initial conditions:

$$\begin{aligned} &\mathbf{u}|_{(t=0)} = \mathbf{u}_0, P|_{(t=0)} = P_0, \phi|_{(t=0)} = \phi_0, T|_{(t=0)} = T_0, \\ &U|_{(t=0)} = U(\phi_0), Q|_{(t=0)} = 1, R|_{(t=0)} = 1. \end{aligned} \tag{3.13}$$

The modified system (3.6)-(3.12), incorporating three auxiliary nonlocal variables U, Q, R, retains its equivalence to the original model (2.2)-(2.5). The terms labeled "Q-reform" and "R-reform" essentially remain unchanged since $Q = 1$ and $R = 1$. Consequently, these specific modifications involving U, Q, R to formulate an equivalent system serve as the foundational "algorithm-friendly" version, crucial for the development of the desired scheme aimed in this study.

Indeed, it is also worth noting that reformulation is a strategy frequently utilized in the design of numerical algorithms, providing effective solutions to a variety of complex challenges. Examples include the modification of advective terms to enhance stability (cf. [1,8]), altering the divergence-free condition to circumvent solving the pressure Poisson equation (cf. [9,23]), and redefining energy potentials as a quadratic form in the context of IEQ/SAV methods (cf. [21,27,28]). The flexibility provided by the "reformulation"

approach is critical in developing the "desired" scheme to solve the highly coupled and nonlinear dendritic phase-field model in this article.

Given that the system (3.6)-(3.12) is equivalent to the original system, it is expected to adhere to the same energy law in Lemma 2.1. However, establishing the energy law for this "algorithm-friendly" version is primarily aimed at guiding the discrete scheme; thus, it remains essential to explicitly demonstrate how the energy law is preserved within the restructured system (3.6)-(3.12). This process is detailed as follows.

Lemma 3.1. *The system,* (3.6)-(3.12)*, upholds the following energy law:*

$$\begin{aligned}\frac{d}{dt}\hat{E}_{tot}(\mathbf{u},\phi,T,U,Q,R) =& -\tau\|\phi_t\|^2-\frac{\lambda D}{\epsilon K}\|\nabla T\|^2\\ &-\nu(\frac{1-\phi}{2}\nabla\mathbf{u},\nabla\mathbf{u})-\nu\xi(q(\phi)\mathbf{u},\mathbf{u}),\end{aligned}\tag{3.14}$$

where

$$\begin{aligned}\hat{E}_{tot}(\mathbf{u},\phi,T,U,Q,R) =& \frac{1}{2}\left\|\frac{1-\phi}{2}\mathbf{u}\right\|^2+\frac{S_1}{2}\|\nabla\phi\|^2+\frac{S_2}{2\epsilon^2}\|\phi\|^2\\ &+\frac{\lambda}{2\epsilon K}\|T\|^2+|U|^2+\frac{|Q|^2}{2}+\frac{|R|^2}{2}-B-1.\end{aligned}\tag{3.15}$$

Proof. By taking the L^2-inner product of (3.6) with $\mathbf{u}$, and using integration by parts and (3.7), we derive

$$\frac{1}{2}\frac{d}{dt}\left\|\frac{1-\phi}{2}\mathbf{u}\right\|^2+\underbrace{R\left(\frac{1-\phi}{2}(\mathbf{u}\cdot\nabla)\mathbf{u},\mathbf{u}\right)}_{\mathrm{I}_1}+\nu(\frac{1-\phi}{2}\nabla\mathbf{u},\nabla\mathbf{u})=-\nu\xi(q(\phi)\mathbf{u},\mathbf{u}).\tag{3.16}$$

By taking the L^2-inner product of (3.8) with ϕ_t and using integration by parts, we get

$$\tau\|\phi_t\|^2+\frac{d}{dt}\left(\frac{S_1}{2}\|\nabla\phi\|^2+\frac{S_2}{2\epsilon^2}\|\phi\|^2\right)=\underbrace{-QU(H,\phi_t)}_{\mathrm{II}_1}\underbrace{-\frac{\lambda}{\epsilon}Q(p(\phi)T,\phi_t)}_{\mathrm{III}_1}.\tag{3.17}$$

By taking the L^2-inner product of (3.9) with $\frac{\lambda}{\epsilon K}T$ and using integration by parts, we obtain

$$\frac{\lambda}{2\epsilon K}\frac{d}{dt}\|T\|^2+\frac{\lambda}{\epsilon K}\underbrace{Q\left(\frac{1-\phi}{2}\mathbf{u}\cdot\nabla T,T\right)}_{\mathrm{IV}_1}=-\frac{\lambda D}{\epsilon K}\|\nabla T\|^2+\underbrace{\frac{\lambda}{\epsilon}Q(p(\phi)\phi_t,T)}_{\mathrm{V}_1}.\tag{3.18}$$

By multiplying (3.10) with $2U$, we get

$$\frac{d}{dt}|U|^2=\underbrace{QU(H,\phi_t)}_{\mathrm{VI}_1}.\tag{3.19}$$

By multiplying (3.11) with Q, we get

$$\begin{aligned}\frac{d}{dt}(\frac{|Q|^2}{2}) =& \underbrace{\frac{\lambda}{\epsilon}Q(p(\phi)T,\phi_t)}_{\mathrm{III}_2}\underbrace{-\frac{\lambda}{\epsilon}Q(p(\phi)\phi_t,T)}_{\mathrm{V}_2}\\ &+\underbrace{QU(H,\phi_t)}_{\mathrm{II}_2}\underbrace{-QU(H,\phi_t)}_{\mathrm{VI}_2}+\underbrace{\frac{\lambda}{\epsilon K}Q\left(\frac{1-\phi}{2}\mathbf{u}\cdot\nabla T,T\right)}_{\mathrm{IV}_2}.\end{aligned}\tag{3.20}$$

By multiplying (3.12) with R, we get

$$\frac{d}{dt}(\frac{|R|^2}{2})=\underbrace{R\left(\frac{1-\phi}{2}(\mathbf{u}\cdot\nabla)\mathbf{u},\mathbf{u}\right)}_{\mathrm{I}_2}.\tag{3.21}$$

By combining (3.16)-(3.21) and recognizing that terms grouped under the same Roman numeral labels, such as I_1 and I_2, cancel each other, we derive the energy dissipation law (3.14). □

Remark 3.1. The difference between Lemma 2.1 and Lemma 3.1 in deriving the energy law emphasizes the rationale for the specific modification from the original system, (2.2)-(2.5), to its new equivalent version, (3.6)-(3.12). This modification is primarily centered around the different methods of cancelling the nonlinear terms. Using the latent heat coupling term $p(\phi)T$ from the original equation (2.4) as an illustrative example, it is significant to note that during the derivation of Lemma 2.1, term II from (2.15) is counteracted by term III from (2.16). This relationship necessitates the careful discretization of $p(\phi)T$ and $p(\phi)\phi_t$ to ensure that these terms effectively negate each other, often resulting in the development of coupled-type numerical algorithms.

However, shown in Lemma 3.1, the process of deriving the energy law for the modified system (3.6)-(3.12) employs a distinctly different approach to cancellation. The terms III_1 in (3.17) and V_1 in (3.18) are not required to nullify each other. Instead, term III_2 in (3.20) effectively cancels out III_1, and similarly, term V_2 in (3.20) negates V_1. This variation allows for different discretization methods to be applied to $Qp(\phi)T$ and $Qp(\phi)\phi_t$ when developing numerical schemes, facilitating the creation of a fully decoupled type scheme.

3.2. Numerical scheme

In this subsection, we design a fully discrete finite element scheme for solving the modified model (3.6)-(3.12), which is the equivalent system of the original model (2.2)-(2.5). The scheme is expected to be the "desired" type, that is, linear, fully decoupled, unconditionally energy stable, and second-order accurate in time. We denote $\delta t > 0$ as a time step size and $t^n = n\delta t$ for $0 \le n \le N$ with $T = N\delta t$. Let ψ^n be the numerical approximation to the function $\psi(\cdot,t)|_{t=t^n}$.

Some finite dimensional discrete subspaces are introduced as follows. Assuming that the polygonal/polyhedral domain Ω is discretized by a conforming and shape regular triangulation/tetrahedron mesh $\mathcal{T}_h$ that is composed by open disjoint elements K such that $\bar{\Omega} = \bigcup_{K\in\mathcal{T}_h} \bar{K}$. We use $\mathcal{P}_l$ to denote the space of polynomials of total degree at most l and define the following finite element spaces:

$$\begin{aligned} Y_h &= \left\{ X \in C^0(\Omega) : X|_K \in \mathcal{P}_{l_1}(K), \forall K \in \mathcal{T}_h \right\}, \\ \boldsymbol{V}_h &= \left\{ \boldsymbol{v} \in C^0(\Omega)^d : \boldsymbol{v}|_K \in \mathcal{P}_{l_2}(K)^d, \forall K \in \mathcal{T}_h \right\} \cap H_0^1(\Omega)^d, \\ O_h &= \left\{ q \in C^0(\Omega) : q|_K \in \mathcal{P}_{l_2-1}(K), \forall K \in \mathcal{T}_h \right\} \cap L_0^2(\Omega), \end{aligned} \tag{3.22}$$

where $H_0^1(\Omega) = \{u \in H^1(\Omega) : u|_{\partial\Omega} = 0\}$ and $L_0^2(\Omega) = \{q \in L^2(\Omega) : \int_\Omega q dx = 0\}$. Hence,

$$Y_h \subset H^1(\Omega), \boldsymbol{V}_h \subset H_0^1(\Omega)^d, O_h \subset L_0^2(\Omega). \tag{3.23}$$

Besides, we assume the pair of spaces $(\boldsymbol{V}_h, O_h)$ satisfy the *inf-sup* condition [7]:

$$\beta\|q\| \le \sup_{\boldsymbol{v}\in\boldsymbol{V}_h} \frac{(\nabla\cdot\boldsymbol{v}, q)}{\|\nabla\boldsymbol{v}\|}, \quad \forall q \in O_h,$$

where the constant β only depends on Ω. A well known *inf-sup* stable pair $(\boldsymbol{V}_h, O_h)$ is the Taylor-Hood element [7].

The semi-discrete formulations of the system (3.6)-(3.12) in the weak form read as: find $(\phi, T, \mathbf{u}, P) \in Y_h \times Y_h \times \boldsymbol{V}_h \times O_h, U \in \mathbb{R}, Q \in \mathbb{R}, R \in \mathbb{R}$, such that

$$\begin{aligned} &\left(\left(\frac{1-\phi}{2}\mathbf{u} \right)_t, \frac{1-\phi}{2}\mathbf{v} \right) + R\left(\frac{1-\phi}{2}(\mathbf{u}\cdot\nabla)\mathbf{u}, \mathbf{v} \right) + \nu\left(\frac{1-\phi}{2}\nabla\mathbf{u}, \nabla\mathbf{v} \right) \\ &\qquad + \left(\frac{1-\phi}{2}\nabla P, \mathbf{v} \right) = -\nu\xi(q(\phi)\mathbf{u}, \mathbf{v}), \end{aligned} \tag{3.24}$$

$$\left(\nabla\cdot\left(\frac{1-\phi}{2}\mathbf{u} \right), q \right) = 0, \tag{3.25}$$

$$\tau(\phi_t, \Phi) + S_1(\nabla\phi, \nabla\Phi) + \frac{S_2}{\epsilon^2}(\phi, \Phi) = -QU(H, \Phi) - \frac{\lambda}{\epsilon}Q(p(\phi)T, \Phi), \tag{3.26}$$

$$(T_t, \Theta) + Q\left(\left(\frac{1-\phi}{2} \right)\mathbf{u}\cdot\nabla T, \Theta \right) = -D(\nabla T, \nabla\Theta) + KQ(p(\phi)\phi_t, \Theta), \tag{3.27}$$

$$U_t = \frac{1}{2}Q(H, \phi_t), \tag{3.28}$$

$$Q_t = \frac{\lambda}{\epsilon}(p(\phi)T, \phi_t) - \frac{\lambda}{\epsilon}(p(\phi)\phi_t, T) + (HU, \phi_t) - (H\phi_t, U) + \frac{\lambda}{\epsilon K}\left(\frac{1-\phi}{2}\mathbf{u}\cdot\nabla T, T \right), \tag{3.29}$$

$$R_t = \left(\frac{1-\phi}{2}(\mathbf{u}\cdot\nabla)\mathbf{u}, \mathbf{u} \right), \tag{3.30}$$

for $(\Phi, \Theta, \mathbf{v}, q) \in Y_h \times Y_h \times \boldsymbol{V}_h \times O_h$.

We now construct the fully discrete scheme as follows. Given that the values of $\phi_h^n, T_h^n, (\psi_h\mathbf{u}_h)^n, P_h^n, U^n, Q^n, R^n$ and $\phi_h^{n-1}, T_h^{n-1}, (\psi_h\mathbf{u}_h)^{n-1}, P_h^{n-1}, U^{n-1}, Q^{n-1}, R^{n-1}$ are known, we update $\phi_h^{n+1}, T_h^{n+1}, \tilde{\mathbf{u}}_h^{n+1}, (\psi_h\mathbf{u}_h)^{n+1}, P_h^{n+1}, U^{n+1}, Q^{n+1}, R^{n+1}$, through the following three-step process:

step 1: find $\phi_h^{n+1} \in Y_h, T_h^{n+1} \in Y_h$, $U^{n+1} \in \mathbb{R}$, $Q^{n+1} \in \mathbb{R}$, such that

$$\tau\left(\frac{a\phi_h^{n+1} - b\phi_h^n + c\phi_h^{n-1}}{2\delta t}, \Phi_h\right) + S_1(\nabla\phi_h^{n+1}, \nabla\Phi_h) + \frac{S_2}{\epsilon^2}(\phi_h^{n+1}, \Phi_h) \tag{3.31}$$
$$= -Q^{n+1}U^*(H^*, \Phi_h) - \frac{\lambda}{\epsilon}Q^{n+1}(p^*T_h^*, \Phi_h),$$

$$\left(\frac{aT_h^{n+1} - bT_h^n + cT_h^{n-1}}{2\delta t}, \Theta_h\right) + Q^{n+1}(\psi_h^*\mathbf{u}_h^* \cdot \nabla T_h^*, \Theta_h) \tag{3.32}$$
$$= -D(\nabla T_h^{n+1}, \nabla\Theta_h) + KQ^{n+1}(p^*\phi_t^*, \Theta_h),$$

$$\frac{aU^{n+1} - bU^n + cU^{n-1}}{2\delta t} = \frac{1}{2}Q^{n+1}(H^*, \phi_t^*), \tag{3.33}$$

$$\frac{aQ^{n+1} - bQ^n + cQ^{n-1}}{2\delta t} = \frac{\lambda}{\epsilon}(p^*T^*, \frac{a\phi_h^{n+1} - b\phi_h^n + c\phi_h^{n-1}}{2\delta t}) - \frac{\lambda}{\epsilon}(p^*\phi_t^*, T_h^{n+1}) \tag{3.34}$$
$$+U^*(H^*, \frac{a\phi_h^{n+1} - b\phi_h^n + c\phi_h^{n-1}}{2\delta t}) - U^{n+1}(H^*, \phi_t^*)$$
$$+\frac{\lambda}{\epsilon K}\left(\psi_h^*\mathbf{u}_h^* \cdot \nabla T_h^*, T_h^{n+1}\right);$$

step 2: find $\tilde{\mathbf{u}}_h^{n+1} \in \boldsymbol{V}_h$, $R^{n+1} \in \mathbb{R}$, such that

$$\left(\frac{a\psi_h^{n+1}\tilde{\mathbf{u}}_h^{n+1} - b\psi_h^n\mathbf{u}_h^n + c\psi_h^{n-1}\mathbf{u}_h^{n-1}}{2\delta t}, \psi_h^{n+1}\mathbf{v}_h\right) + R^{n+1}(\psi_h^*(\mathbf{u}_h^* \cdot \nabla)\mathbf{u}_h^*, \mathbf{v}_h) \tag{3.35}$$
$$+\nu(\psi_h^{n+1}\nabla\tilde{\mathbf{u}}_h^{n+1}, \nabla\mathbf{v}_h) + (\psi_h^{n+1}\nabla P_h^n, \mathbf{v}_h) = -\nu\xi(q(\hat{\phi}_h^{n+1})\tilde{\mathbf{u}}^{n+1}, \mathbf{v}_h),$$

$$\frac{aR^{n+1} - bR^n + cR^{n-1}}{2\delta t} = \left(\psi_h^*(\mathbf{u}_h^* \cdot \nabla)\mathbf{u}_h^*, \tilde{\mathbf{u}}_h^{n+1}\right); \tag{3.36}$$

step 3: find $P_h^{n+1} \in O_h$, such that

$$(\nabla(P_h^{n+1} - P_h^n), \nabla q_h) = -\frac{a}{2\delta t}(\nabla \cdot (\psi_h^{n+1}\tilde{\mathbf{u}}_h^{n+1}), q_h), \tag{3.37}$$

$$\psi_h^{n+1}\mathbf{u}_h^{n+1} = \psi_h^{n+1}\tilde{\mathbf{u}}_h^{n+1} - \frac{2\delta t}{a}(\nabla P_h^{n+1} - \nabla P_h^n), \tag{3.38}$$

where

$$\begin{cases} a = 3, b = 4, c = 1, \tilde{a} = 5, \tilde{b} = 8, \tilde{c} = 3, \\ \phi_h^* = 2\phi_h^n - \phi_h^{n-1}, T_h^* = 2T_h^n - T_h^{n-1}, \mathbf{u}_h^* = 2\mathbf{u}_h^n - \mathbf{u}_h^{n-1}, U^* = 2U^n - U^{n-1}, \\ H^* = H(\phi_h^*), p^* = p(\phi_h^*), \\ \hat{\phi}_h = \begin{cases} 1-\varepsilon, & \phi_h \in (1-\varepsilon, \infty), \\ \phi_h, & \phi_h \in [-1+\varepsilon, 1-\varepsilon], \\ -1+\varepsilon, & \phi_h \in (-\infty, -1+\varepsilon), \end{cases} 0 < \varepsilon \ll 1, \\ \psi_h^n = \dfrac{1-\hat{\phi}_h^n}{2}, \psi_h^* = 2\psi_h^n - \psi_h^{n-1}, \phi_t^* = \dfrac{\tilde{a}\phi_h^n - \tilde{b}\phi_h^{n-1} + \tilde{c}\phi_h^{n-2}}{2\delta t}. \end{cases} \tag{3.39}$$

Several remarks are given to explain the scheme (3.31)-(3.38).

Remark 3.2. In the design of the above discretization approach, we skillfully combine explicit and implicit treatments to deal with nonlinear terms. For those terms involving nonlocal variables Q and R, the implicit treatment is used to discretize Q and R, while explicit treatment is used to discretize others (such as $Q^{n+1}p^*T_h^*$ in (3.31)). This hybrid discretization approach is instrumental in achieving a fully decoupled scheme.

Moreover, we employ the SAV method to convert the nonlinear portion of the free energy into a quadratic form (i.e., U^2), introducing a novel nonlocal variable U to facilitate the linearization of nonlinear terms. But our approach diverges from the SAV approach by applying a purely explicit treatment to the resultant nonlinear term HU (see H^*U^* in (3.31)), whereas the SAV method usually discretizes it as H^*U^{n+1}. To underscore this distinction, we refer to our methodology as the explicit-SAV method.

Remark 3.3. We develop a projection-type approach to facilitate the decoupling of velocity field and pressure computations. The projection method has undergone extensive analysis for traditional Navier-Stokes equations that do not include a weight factor, see the detailed analysis in [3,19]. Following a comparable way, when solving the fluid momentum equation with the weight factor, the intermediate velocity $\tilde{\mathbf{u}}_h^{n+1}$ is first obtained in step 2, and then it is projected onto the divergence-free space. It's important to highlight

that the velocity form resulting from the projection step consistently encompasses this weight factor due to the specific form of the divergence-free condition.

Additionally, in the context of traditional Navier-Stokes equations, it has been established that the projection-type approach can achieve second-order temporal accuracy for the velocity field while being limited to first-order accuracy for the pressure. The diminished precision in pressure is associated with the imposition of homogeneous Neumann-type boundary conditions to the pressure, thoroughly discussed in [6]. The proposed scheme numerically exhibits the same behavior, as detailed by numerical tests in Section 4.

Remark 3.4. The final velocity field with the weight factor, $\psi^{n+1}\mathbf{u}_h^{n+1}$, can be demonstrated to satisfy the divergence-free condition in a discrete manner. Namely, by taking the L^2-inner product of (3.37) with $\nabla q_h, q_h \in O_h$, we get

$$(\psi_h^{n+1}\mathbf{u}_h^{n+1}, \nabla q_h) = (\psi_h^{n+1}\tilde{\mathbf{u}}_h^{n+1}, \nabla q_h) - \frac{2\delta t}{a}(\nabla(P_h^{n+1} - P_h^n), \nabla q_h). \tag{3.40}$$

Hence, from (3.37), we derive

$$(\psi_h^{n+1}\mathbf{u}_h^{n+1}, \nabla q_h) = 0. \tag{3.41}$$

Remark 3.5. In implementation, the initial values required for startup are typically derived using first-order schemes, such as the one developed in [4]. Alternatively, one can simply set $a = \tilde{a} = 2, b = \tilde{b} = 2, c = \tilde{c} = 0$ in the developed scheme (3.31)-(3.38). A small constant ε is introduced to restrict the value of ϕ to the interval $[-1+\varepsilon, 1-\varepsilon]$, where $0 < \varepsilon \ll 1$. Consequently, this ensures that the range of ψ^k consistently falls within $[\frac{\epsilon}{2}, 1-\frac{\epsilon}{2}]$, which in turn guarantees the solvability of (3.35), see the implementation of step 2 in Section 3.4.

Remark 3.6. Due to the term H^*, which comprises a significant number of explicitly treated nonlinear and second-order spatial terms, the stabilization terms associated with S_1 and S_2 in (3.31) are crucial in ensuring the H^1-stability of ϕ. Explicit treatment of nonlinear terms is well-known for potentially causing instability. To counter this, using linear terms as stabilizers, which match the spatial order of the nonlinear terms, is a widely recognized approach, underlying the incorporation of the S_1 term. Similarly, the S_2 term is used to offset the explicitly handled term $f(\phi)$ within H^*. For an extensive review of linear stabilization techniques in the context of gradient flow models, especially those characterized by considerable stiffness, we refer to [24].

3.3. Energy stability

We now proceed to demonstrate that the scheme (3.31)-(3.38) possesses unconditional energy stability and adheres to the energy dissipative structure at the discrete level.

Theorem 3.1. *The scheme* (3.31)-(3.38) *complies the discrete energy law, which reads as:*

$$\begin{aligned}\frac{1}{\delta t}(E^{n+1} - E^n) \le & -\frac{\lambda D}{\epsilon K}\|\nabla T_h^{n+1}\|^2 - \tau\left\|\frac{3\phi_h^{n+1} - 4\phi_h^n + \phi_h^{n-1}}{2\delta t}\right\|^2 \\ & - \nu\|\sqrt{\psi_h^{n+1}}\nabla\tilde{\mathbf{u}}_h^{n+1}\|^2 - \nu\xi\|\sqrt{q(\hat{\phi}_h^{n+1})}\tilde{\mathbf{u}}_h^{n+1}\|^2 \le 0,\end{aligned} \tag{3.42}$$

where

$$\begin{aligned}E^{n+1} = & \frac{1}{2}(\frac{1}{2}\|\psi_h^{n+1}\mathbf{u}_h^{n+1}\|^2 + \frac{1}{2}\|2\psi_h^{n+1}\mathbf{u}_h^{n+1} - \psi_h^n\mathbf{u}_h^n\|^2) + \frac{\delta t}{3}\|\nabla P_h^{n+1}\|^2 \\ & + \frac{S_1}{2}(\frac{1}{2}\|\nabla\phi_h^{n+1}\|^2 + \frac{1}{2}\|2\nabla\phi_h^{n+1} - \nabla\phi_h^n\|^2) + \frac{S_2}{2\epsilon^2}(\frac{1}{2}\|\phi_h^{n+1}\|^2 + \frac{1}{2}\|2\phi_h^{n+1} - \phi_h^n\|^2) \\ & + \frac{\lambda}{2\epsilon K}(\frac{1}{2}\|T_h^{n+1}\|^2 + \frac{1}{2}\|2T_h^{n+1} - T_h^n\|^2) + (\frac{1}{2}|U^{n+1}|^2 + \frac{1}{2}|2U^{n+1} - U^n|^2) \\ & + \frac{1}{2}(\frac{1}{2}|Q^{n+1}|^2 + \frac{1}{2}|2Q^{n+1} - Q^n|^2) + \frac{1}{2}(\frac{1}{2}|R^{n+1}|^2 + \frac{1}{2}|2R^{n+1} - R^n|^2) - B - 1.\end{aligned} \tag{3.43}$$

Proof. By setting $\mathbf{v}_h = 2\delta t\tilde{\mathbf{u}}_h^{n+1}$ in (3.35), we obtain

$$\begin{aligned}(3\psi_h^{n+1}\tilde{\mathbf{u}}_h^{n+1} - 4\psi_h^n\mathbf{u}_h^n + \psi_h^{n-1}\mathbf{u}_h^{n-1}, \psi_h^{n+1}\tilde{\mathbf{u}}_h^{n+1}) + 2\nu\delta t(\psi_h^{n+1}\nabla\tilde{\mathbf{u}}_h^{n+1}, \nabla\tilde{\mathbf{u}}_h^{n+1}) \\ + 2\delta t(\psi_h^{n+1}\nabla P_h^n, \tilde{\mathbf{u}}_h^{n+1}) = -2\delta t R^{n+1}(\psi^*(\mathbf{u}^*\cdot\nabla)\mathbf{u}^*, \tilde{\mathbf{u}}_h^{n+1}) \\ - 2\delta t\nu\xi(q(\hat{\phi}_h^{n+1})\tilde{\mathbf{u}}_h^{n+1}, \tilde{\mathbf{u}}_h^{n+1}).\end{aligned} \tag{3.44}$$

We rewrite (3.38) as

$$\psi_h^{n+1}\tilde{\mathbf{u}}_h^{n+1} - \psi_h^{n+1}\mathbf{u}_h^{n+1} = \frac{2\delta t}{3}\nabla(P_h^{n+1} - P_h^n). \tag{3.45}$$

Taking the L^2-inner product of the above equality with $\psi_h^{n+1}\mathbf{u}_h^{n+1}$ and using (3.41), we derive

$$(\psi_h^{n+1}\tilde{\mathbf{u}}_h^{n+1} - \psi_h^{n+1}\mathbf{u}_h^{n+1}, \psi_h^{n+1}\mathbf{u}_h^{n+1}) = \frac{2\delta t}{3}(\nabla(P_h^{n+1} - P_h^n), \psi_h^{n+1}\mathbf{u}_h^{n+1}) = 0. \tag{3.46}$$

Using (3.46), we derive

$$\begin{aligned}
&(3\psi_h^{n+1}\tilde{\mathbf{u}}_h^{n+1} - 4\psi_h^n\mathbf{u}_h^n + \psi_h^{n-1}\mathbf{u}_h^{n-1}, \psi_h^{n+1}\tilde{\mathbf{u}}_h^{n+1}) \\
&\quad = (3\psi_h^{n+1}\tilde{\mathbf{u}}_h^{n+1} - 4\psi_h^n\mathbf{u}_h^n + \psi_h^{n-1}\mathbf{u}_h^{n-1}, \psi_h^{n+1}\mathbf{u}_h^{n+1}) \\
&\qquad + (3\psi_h^{n+1}\tilde{\mathbf{u}}_h^{n+1} - 4\psi_h^n\mathbf{u}_h^n + \psi_h^{n-1}\mathbf{u}_h^{n-1}, \psi_h^{n+1}\tilde{\mathbf{u}}_h^{n+1} - \psi_h^{n+1}\mathbf{u}_h^{n+1}) \\
&\quad = (3\psi_h^{n+1}\mathbf{u}_h^{n+1} - 4\psi_h^n\mathbf{u}_h^n + \psi_h^{n-1}\mathbf{u}_h^{n-1}, \psi_h^{n+1}\mathbf{u}_h^{n+1}) \\
&\qquad + (3\psi_h^{n+1}\tilde{\mathbf{u}}_h^{n+1},\ \psi_h^{n+1}\tilde{\mathbf{u}}_h^{n+1} - \psi_h^{n+1}\mathbf{u}_h^{n+1}) \\
&\quad = (3\psi_h^{n+1}\mathbf{u}_h^{n+1} - 4\psi_h^n\mathbf{u}_h^n + \psi_h^{n-1}\mathbf{u}_h^{n-1}, \psi_h^{n+1}\mathbf{u}_h^{n+1}) \\
&\qquad + 3(\psi_h^{n+1}\tilde{\mathbf{u}}_h^{n+1} - \psi_h^{n+1}\mathbf{u}_h^{n+1}, \psi_h^{n+1}\tilde{\mathbf{u}}_h^{n+1} + \psi_h^{n+1}\mathbf{u}_h^{n+1}) \\
&\quad = \frac{1}{2}\Big(\|\psi_h^{n+1}\mathbf{u}_h^{n+1}\|^2 - \|\psi_h^n\mathbf{u}_h^n\|^2 + \|2\psi_h^{n+1}\mathbf{u}_h^{n+1} - \psi_h^n\mathbf{u}^n\|^2 - \|2\psi_h^n\mathbf{u}_h^n - \psi_h^{n-1}\mathbf{u}_h^{n-1}\|^2 \\
&\qquad + \|\psi_h^{n+1}\mathbf{u}_h^{n+1} - 2\psi_h^n\mathbf{u}_h^n + \psi_h^{n-1}\mathbf{u}_h^{n-1}\|^2\Big) + 3(\|\psi_h^{n+1}\tilde{\mathbf{u}}_h^{n+1}\|^2 - \|\psi_h^{n+1}\mathbf{u}_h^{n+1}\|^2),
\end{aligned} \tag{3.47}$$

where the last equality is derived using the following identity

$$2a(3a - 4b + c) = a^2 - b^2 + (2a - b)^2 - (2b - c)^2 + (a - 2b + c)^2. \tag{3.48}$$

We reformulate the projection step (3.38) as

$$\frac{3}{2\delta t}\psi_h^{n+1}\mathbf{u}_h^{n+1} + \nabla P_h^{n+1} = \frac{3}{2\delta t}\psi_h^{n+1}\tilde{\mathbf{u}}_h^{n+1} + \nabla P_h^n. \tag{3.49}$$

Taking the L^2-inner product of the above equation with itself, we derive

$$\frac{9}{4\delta t^2}\|\psi_h^{n+1}\mathbf{u}_h^{n+1}\|^2 + \|\nabla P_h^{n+1}\|^2 = \frac{9}{4\delta t^2}\|\psi_h^{n+1}\tilde{\mathbf{u}}_h^{n+1}\|^2 + \|\nabla P_h^n\|^2 + \frac{3}{\delta t}(\psi_h^{n+1}\tilde{\mathbf{u}}_h^{n+1}, \nabla P_h^n). \tag{3.50}$$

Hence, by multiplying $2\delta t^2/3$ to the above equation, we derive

$$\frac{3}{2}(\|\psi_h^{n+1}\mathbf{u}_h^{n+1}\|^2 - \|\psi_h^{n+1}\tilde{\mathbf{u}}_h^{n+1}\|^2) + \frac{2\delta t^2}{3}(\|\nabla P_h^{n+1}\|^2 - \|\nabla P_h^n\|^2) = 2\delta t(\psi_h^{n+1}\tilde{\mathbf{u}}_h^{n+1}, \nabla P_h^n). \tag{3.51}$$

We rewrite (3.38) again as

$$\psi_h^{n+1}\mathbf{u}_h^{n+1} - \psi_h^{n+1}\tilde{\mathbf{u}}_h^{n+1} = -\frac{2}{3}\delta t\nabla P_h^{n+1} + \frac{2}{3}\delta t\nabla P_h^n. \tag{3.52}$$

By taking the L^2-inner product of (3.52) with $\frac{3}{2}\psi_h^{n+1}\mathbf{u}_h^{n+1}$ and using (3.41), we derive

$$\frac{3}{2}(\|\psi_h^{n+1}\mathbf{u}_h^{n+1}\|^2 - \|\psi_h^{n+1}\tilde{\mathbf{u}}_h^{n+1}\|^2 + \|\psi_h^{n+1}\mathbf{u}_h^{n+1} - \psi_h^{n+1}\tilde{\mathbf{u}}_h^{n+1}\|^2) = 0. \tag{3.53}$$

We combine (3.44), (3.47), (3.51), and (3.53) to obtain

$$\begin{aligned}
&\frac{1}{2}(\|\psi_h^{n+1}\mathbf{u}_h^{n+1}\|^2 + \|2\psi_h^{n+1}\mathbf{u}_h^{n+1} - \psi_h^n\mathbf{u}_h^n\|^2) - \frac{1}{2}(\|\psi_h^n\mathbf{u}_h^n\|^2 - \|2\psi_h^n\mathbf{u}_h^n - \psi_h^{n-1}\mathbf{u}_h^{n-1}\|^2) \\
&\qquad + \frac{1}{2}\|\psi_h^{n+1}\mathbf{u}_h^{n+1} - 2\psi_h^n\mathbf{u}_h^n + \psi_h^{n-1}\mathbf{u}_h^{n-1}\|^2 + \frac{3}{2}\|\psi_h^{n+1}\mathbf{u}_h^{n+1} - \psi_h^{n+1}\tilde{\mathbf{u}}_h^{n+1}\|^2 \\
&\qquad + \frac{2\delta t^2}{3}(\|\nabla P_h^{n+1}\|^2 - \|\nabla P_h^n\|^2) \\
&\qquad = -2\delta t\nu\|\sqrt{\psi_h^{n+1}}\nabla\tilde{\mathbf{u}}_h^{n+1}\|^2 - 2\delta t\nu\xi\|\sqrt{q(\hat{\phi}_h^{n+1})}\tilde{\mathbf{u}}_h^{n+1}\|^2 \\
&\qquad\quad \underbrace{-2\delta t R^{n+1}(\psi_h^*(\mathbf{u}_h^*\cdot\nabla)\mathbf{u}_h^*, \tilde{\mathbf{u}}_h^{n+1})}_{\mathrm{I}_1}.
\end{aligned} \tag{3.54}$$

By taking $\Phi_h = 3\phi_h^{n+1} - 4\phi_h^n + \phi_h^{n-1}$ in (3.31), we obtain

$$\begin{aligned}
&2\delta t\tau\left\|\frac{3\phi_h^{n+1} - 4\phi_h^n + \phi_h^{n-1}}{2\delta t}\right\|^2 \\
&+S_1(\frac{1}{2}\|\nabla\phi_h^{n+1}\|^2 + \frac{1}{2}\|2\nabla\phi_h^{n+1} - \nabla\phi_h^n\|^2) - S_1(\frac{1}{2}\|\nabla\phi_h^n\|^2 + \frac{1}{2}\|2\nabla\phi_h^n - \nabla\phi_h^{n-1}\|^2) \\
&+\frac{S_2}{\epsilon^2}(\frac{1}{2}\|\phi_h^{n+1}\|^2 + \frac{1}{2}\|2\phi_h^{n+1} - \phi_h^n\|^2) - \frac{S_2}{\epsilon^2}(\frac{1}{2}\|\phi_h^n\|^2 + \frac{1}{2}\|2\phi_h^n - \phi_h^{n-1}\|^2)
\end{aligned} \tag{3.55}$$

$$+S_1\frac{1}{2}\|\nabla\phi_h^{n+1}-2\nabla\phi_h^n+\nabla\phi_h^{n-1}\|^2+\frac{S_2}{\epsilon^2}\frac{1}{2}\|\phi_h^{n+1}-2\phi_h^n+\phi_h^{n-1}\|^2$$
$$=\underbrace{-Q^{n+1}U^*(H^*,3\phi_h^{n+1}-4\phi_h^n+\phi_h^{n-1})}_{\mathrm{II}_1}\underbrace{-\frac{\lambda}{\epsilon}Q^{n+1}(p^*T_h^*,3\phi_h^{n+1}-4\phi_h^n+\phi_h^{n-1})}_{\mathrm{III}_1}.$$

By setting $\Theta_h=2\delta t\frac{\lambda}{\epsilon K}T_h^{n+1}$ in (3.32), and using (3.48), we obtain

$$\begin{aligned}\frac{\lambda}{\epsilon K}\Big(\frac{1}{2}\|T_h^{n+1}\|^2+\frac{1}{2}\|2T_h^{n+1}-T_h^n\|^2\Big)-\frac{\lambda}{\epsilon K}\Big(\frac{1}{2}\|T_h^n\|^2+\frac{1}{2}\|2T_h^n-T_h^{n-1}\|^2\Big)\\+\frac{\lambda}{2\epsilon K}\|T_h^{n+1}-2T_h^n+T_h^{n-1}\|^2+\underbrace{2\delta t\frac{\lambda}{\epsilon K}Q^{n+1}(\psi_h^*\mathbf{u}_h^*\cdot\nabla T_h^*,T_h^{n+1})}_{\mathrm{IV}_1}\\=-2\frac{\lambda D}{\epsilon K}\delta t\|\nabla T_h^{n+1}\|^2+\underbrace{2\delta t\frac{\lambda}{\epsilon}Q^{n+1}(p^*\phi_t^*,T_h^{n+1})}_{\mathrm{V}_1}.\end{aligned}\tag{3.56}$$

By multiplying (3.33) with $4\delta tU^{n+1}$ and using (3.48), we obtain

$$\begin{aligned}(|U^{n+1}|^2+|2U^{n+1}-U^n|^2)-(|U^n|^2+|2U^n-U^{n-1}|^2)+|U^{n+1}-2U^n+U^{n-1}|^2\\=\underbrace{2\delta tQ^{n+1}U^{n+1}(H^*,\phi_t^*)}_{\mathrm{VI}_1}.\end{aligned}\tag{3.57}$$

By multiplying (3.34) with $2\delta tQ^{n+1}$ and using (3.48), we get

$$\begin{aligned}(\frac{1}{2}|Q^{n+1}|^2+\frac{1}{2}|2Q^{n+1}-Q^n|^2)-(\frac{1}{2}|Q^n|^2+\frac{1}{2}|2Q^n-Q^{n-1}|^2)+\frac{1}{2}|Q^{n+1}-2Q^n+Q^{n-1}|^2\\=\underbrace{\frac{\lambda}{\epsilon}Q^{n+1}(p^*T_h^*,3\phi_h^{n+1}-4\phi_h^n+\phi_h^{n-1})}_{\mathrm{III}_2}\underbrace{-2\delta t\frac{\lambda}{\epsilon}Q^{n+1}(p^*\phi_t^*,T_h^{n+1})}_{\mathrm{V}_2}\\+\underbrace{Q^{n+1}U^*(H^*,3\phi_h^{n+1}-4\phi_h^n+\phi_h^{n-1})}_{\mathrm{II}_2}\underbrace{-2\delta tQ^{n+1}U^{n+1}(H^*,\phi_t^*)}_{\mathrm{VI}_2}\\+\underbrace{2\delta t\frac{\lambda}{\epsilon K}Q^{n+1}\left(\psi_h^*\mathbf{u}_h^*\cdot\nabla T_h^*,T_h^{n+1}\right)}_{\mathrm{IV}_2}.\end{aligned}\tag{3.58}$$

By multiplying (3.36) with $2\delta tR^{n+1}$, we get

$$\begin{aligned}(\frac{1}{2}|R^{n+1}|^2+\frac{1}{2}|2R^{n+1}-R^n|^2)-(\frac{1}{2}|R^n|^2+\frac{1}{2}|2R^n-R^{n-1}|^2)+\frac{1}{2}|R^{n+1}-2R^n+R^{n-1}|^2\\=\underbrace{2\delta tR^{n+1}\left(\psi_h^*(\mathbf{u}_h^*\cdot\nabla)\mathbf{u}_h^*,\tilde{\mathbf{u}}_h^{n+1}\right)}_{\mathrm{I}_2}.\end{aligned}\tag{3.59}$$

Finally, by combining (3.54), (3.55), (3.56), (3.57), (3.58) and (3.59), we obtain

$$\begin{aligned}&\frac{1}{2}(\|\psi_h^{n+1}\mathbf{u}_h^{n+1}\|^2+\|2\psi_h^{n+1}\mathbf{u}_h^{n+1}-\psi_h^n\mathbf{u}_h^n\|^2)-\frac{1}{2}(\|\psi_h^n\mathbf{u}_h^n\|^2-\|2\psi_h^n\mathbf{u}_h^n-\psi_h^{n-1}\mathbf{u}_h^{n-1}\|^2)\\&+\frac{2\delta t^2}{3}(\|\nabla P_h^{n+1}\|^2-\|\nabla P_h^n\|^2)\\&+S_1(\frac{1}{2}\|\nabla\phi_h^{n+1}\|^2+\frac{1}{2}\|2\nabla\phi_h^{n+1}-\nabla\phi_h^n\|^2)-S_1(\frac{1}{2}\|\nabla\phi_h^n\|^2+\frac{1}{2}\|2\nabla\phi_h^n-\nabla\phi_h^{n-1}\|^2)\\&+\frac{S_2}{\epsilon^2}(\frac{1}{2}\|\phi_h^{n+1}\|^2+\frac{1}{2}\|2\phi_h^{n+1}-\phi_h^n\|^2)-\frac{S_2}{\epsilon^2}(\frac{1}{2}\|\phi_h^n\|^2+\frac{1}{2}\|2\phi_h^n-\phi_h^{n-1}\|^2)\\&+\frac{\lambda}{\epsilon K}\Big(\frac{1}{2}\|T_h^{n+1}\|^2+\frac{1}{2}\|2T_h^{n+1}-T_h^n\|^2\Big)-\frac{\lambda}{\epsilon K}\Big(\frac{1}{2}\|T_h^n\|^2+\frac{1}{2}\|2T_h^n-T_h^{n-1}\|^2\Big)\\&+(|U^{n+1}|^2+|2U^{n+1}-U^n|^2)-(|U^n|^2+|2U^n-U^{n-1}|^2)\\&+(\frac{1}{2}|Q^{n+1}|^2+\frac{1}{2}|2Q^{n+1}-Q^n|^2)-(\frac{1}{2}|Q^n|^2+\frac{1}{2}|2Q^n-Q^{n-1}|^2)\\&+(\frac{1}{2}|R^{n+1}|^2+\frac{1}{2}|2R^{n+1}-R^n|^2)-(\frac{1}{2}|R^n|^2+\frac{1}{2}|2R^n-R^{n-1}|^2)+G\end{aligned}\tag{3.60}$$

$$= -2\delta t\frac{\lambda D}{\epsilon K}\|\nabla T_h^{n+1}\|^2 - 2\delta t\tau\left\|\frac{3\phi_h^{n+1}-4\phi_h^n+\phi_h^{n-1}}{2\delta t}\right\|^2$$
$$-2\delta t\nu\|\sqrt{\psi_h^{n+1}}\nabla\tilde{\mathbf{u}}_h^{n+1}\|^2 - 2\delta t\nu\xi\|\sqrt{q(\hat{\phi}_h^{n+1})}\tilde{\mathbf{u}}_h^{n+1}\|^2,$$

where

$$\begin{aligned} G =& \|\psi_h^{n+1}\mathbf{u}_h^{n+1} - 2\psi_h^n\mathbf{u}_h^n + \psi_h^{n-1}\mathbf{u}_h^{n-1}\|^2 + \frac{3}{2}\|\psi_h^{n+1}\mathbf{u}_h^{n+1} - \psi_h^{n+1}\tilde{\mathbf{u}}_h^{n+1}\|^2 \\ &+ S_1\frac{1}{2}\|\nabla\phi_h^{n+1} - 2\nabla\phi_h^n + \nabla\phi_h^{n-1}\|^2 + \frac{S_2}{\epsilon^2}\frac{1}{2}\|\phi_h^{n+1} - 2\phi_h^n + \phi_h^{n-1}\|^2 \\ &+ \frac{\lambda}{4\epsilon K}\|T_h^{n+1} - 2T_h^n + T_h^{n-1}\|^2 + \frac{1}{2}|U^{n+1} - 2U^n + U^{n-1}|^2 \\ &+ \frac{1}{2}|Q^{n+1} - 2Q^n + Q^{n-1}|^2 + \frac{1}{2}|R^{n+1} - 2R^n + R^{n-1}|^2. \end{aligned} \tag{3.61}$$

The desired result (3.42) is obtained after we divide (3.60) with $2\delta t$ and drop the term G (since it is positive). □

Remark 3.7. It should be noted that $\frac{1}{\delta t}(E^{n+1}-E^n)$ serves as a second-order temporal approximation of the term $\frac{d}{dt}\hat{E}_{tot}(\mathbf{u},\phi,T,U,Q,R)$, specifically at the discrete time $t=t^{n+1}$. Since for any smooth variable ψ with time, we always have the following heuristic approximations as

$$\begin{aligned} &\frac{\|\psi^{n+1}\|^2 + \|2\psi^{n+1}-\psi^n\|^2}{2\delta t} - \frac{\|\psi^n\|^2 + \|2\psi^n - \psi^{n-1}\|^2}{2\delta t} \\ &\qquad \cong \frac{\|\psi^{n+2}\|^2 - \|\psi^n\|^2}{2\delta t} + O(\delta t^2) \cong \frac{d}{dt}\|\psi(t^{n+1})\|^2 + O(\delta t^2). \end{aligned} \tag{3.62}$$

3.4. Decoupled-type implementation

This subsection introduces a nonlocal splitting method, which simplifies the process of implementing the decoupling in the scheme (3.31)-(3.38).

Implementation of Step 1: we decompose ϕ_h^{n+1}, T_h^{n+1}, and U^{n+1} into a form consisting of linear combinations, utilizing the nonlocal variable Q^{n+1}, namely,

$$\begin{cases} \phi_h^{n+1} = \phi_{h1}^{n+1} + Q^{n+1}\phi_{h2}^{n+1}, \\ T_h^{n+1} = T_{h1}^{n+1} + Q^{n+1}T_{h2}^{n+1}, \\ U^{n+1} = U_1^{n+1} + Q^{n+1}U_2^{n+1}. \end{cases} \tag{3.63}$$

We solve $\phi_{h1}^{n+1}, \phi_{h2}^{n+1}, T_{h1}^{n+1}, T_{h2}^{n+1}, U_1^{n+1}, U_2^{n+1}$ as follows. After replacing ϕ_h^{n+1}, T_h^{n+1} in (3.31)-(3.32) with (3.63), we decompose the obtained equations into the following four sub-equations according to the nonlocal variable Q^{n+1}:

$$\begin{cases} \frac{3\tau}{2\delta t}(\phi_{h1}^{n+1},\Phi_h) + S_1(\nabla\phi_{h1}^{n+1},\nabla\Phi_h) + \frac{S_2}{\epsilon^2}(\phi_{h1}^{n+1},\Phi_h) = \frac{\tau}{2\delta t}((4\phi_h^n - \phi_h^{n-1}),\Phi_h), \\ \frac{3\tau}{2\delta t}(\phi_{h2}^{n+1},\Phi_h) + S_1(\nabla\phi_{h2}^{n+1},\nabla\Phi_h) + \frac{S_2}{\epsilon^2}(\phi_{h2}^{n+1},\Phi_h) = (-H^*U^* - \frac{\lambda}{\epsilon}p^*T^*,\Phi_h), \\ \frac{3}{2\delta t}(T_{h1}^{n+1},\Theta_h) + D(\nabla T_{h1}^{n+1},\nabla\Theta_h) = (\frac{1}{2\delta t}(4T_h^n - T_h^{n-1}),\Theta_h), \\ \frac{3}{2\delta t}(T_{h2}^{n+1},\Theta_h) + D(\nabla T_{h2}^{n+1},\nabla\Theta_h) = (-\psi_h^*\mathbf{u}_h^*\cdot\nabla T_h^* + Kp^*\phi_t^*,\Theta_h). \end{cases} \tag{3.64}$$

Solving for $\phi_{h1}^{n+1}, \phi_{h2}^{n+1}, T_{h1}^{n+1}, T_{h2}^{n+1}$ from (3.64) is straightforward, as these are merely second-order elliptic equations characterized by constant coefficients.

Similarly, using (3.63), we decompose the equation (3.33) according to Q^{n+1} to obtain the direct solution of U_1^{n+1}, U_2^{n+1}, which read as

$$U_1^{n+1} = \frac{1}{3}(4U^n - U^{n-1}), \quad U_2^{n+1} = \frac{\delta t}{3}(H^*,\phi_t^*). \tag{3.65}$$

We continue to solve Q^{n+1} from (3.34). Utilizing the linear combination forms for the variables ϕ_h^{n+1}, T_h^{n+1}, U^{n+1} in (3.63), we reformulate (3.34) into the subsequent form:

$$(\frac{3}{2\delta t} - \eta_2)Q^{n+1} = \frac{1}{2\delta t}(4Q^n - Q^{n-1}) + \eta_1, \tag{3.66}$$

where $\eta_i, i = 1, 2$ are given as

$$\begin{cases} \eta_1 = \frac{\lambda}{\epsilon}(p^*T_h^*, \frac{3\phi_{h1}^{n+1} - 4\phi_h^n + \phi_h^{n-1}}{2\delta t}) - \frac{\lambda}{\epsilon}(p^*\phi_t^*, T_{h1}^{n+1}), \\ \qquad + U^*(H^*, \frac{3\phi_{h1}^{n+1} - 4\phi_h^n + \phi_h^{n-1}}{2\delta t}) - U_1^{n+1}(H^*, \phi_t^*) + \frac{\lambda}{\epsilon K}(\psi_h^*\mathbf{u}_h^* \cdot \nabla T_h^*, T_{h1}^{n+1}), \\ \eta_2 = \frac{\lambda}{\epsilon}(p^*T_h^*, \frac{3\phi_{h2}^{n+1}}{2\delta t}) - \frac{\lambda}{\epsilon}(p^*\phi_t^*, T_{h2}^{n+1}) \\ \qquad + U^*(H^*, \frac{3\phi_{h2}^{n+1}}{2\delta t}) - U_2^{n+1}(H^*, \phi_t^*) + \frac{\lambda}{\epsilon K}(\psi_h^*\mathbf{u}_h^* \cdot \nabla T_h^*, T_{h2}^{n+1}). \end{cases} \tag{3.67}$$

It is very easy to solve (3.66) since all terms contained in η_1 and η_2 are already obtained previously.

One important issue is the solvability of (3.66), which can be illustrated by showing $\frac{3}{2\delta t} - \eta_2 \neq 0$ as follows.

We set $\Phi_h = \frac{3}{2\delta t}\phi_{h2}^{n+1}$ in the second equation of (3.64) to deduce

$$\begin{aligned} -(H^*U^*, \frac{3\phi_{h2}^{n+1}}{2\delta t}) - \frac{\lambda}{\epsilon}(p^*T_h^*, \frac{3\phi_{h2}^{n+1}}{2\delta t}) = \frac{9\tau}{4\delta t^2}\|\phi_{h2}^{n+1}\|^2 + \frac{3S_1}{2\delta t}\|\nabla\phi_{h2}^{n+1}\|^2 \\ + \frac{3S_2}{\epsilon^2 2\delta t}\|\phi_{h2}^{n+1}\|^2 \geq 0. \end{aligned} \tag{3.68}$$

By multiplying the second equation in (3.65) with $\frac{3}{\delta t}U_2^{n+1}$, we get

$$U_2^{n+1}(H^*, \phi_t^*) = \frac{3}{\delta t}|U_2^{n+1}|^2 \geq 0. \tag{3.69}$$

By setting $\Phi_h = \frac{\lambda}{\epsilon K}T_{h2}^{n+1}$ in the fourth equation of (3.64), we get

$$\frac{\lambda}{\epsilon}(p^*\phi_t^*, T_{h2}^{n+1}) - \frac{\lambda}{\epsilon K}(\psi_h^*\mathbf{u}_h^* \cdot \nabla T_h^*, T_{h2}^{n+1}) = \frac{3\lambda}{2\epsilon K\delta t}\|T_{h2}^{n+1}\|^2 + \frac{\lambda D}{\epsilon K}\|\nabla T_{h2}^{n+1}\|^2 \geq 0. \tag{3.70}$$

The combination of (3.68), (3.69) and (3.70) gives the fact of $-\eta_2 \geq 0$. Thus (3.66) is always solvable. After Q^{n+1} is obtained, we proceed to update $\phi_h^{n+1}, T_h^{n+1}, U^{n+1}$ according to (3.63).

Implementation of Step 2: we split $\tilde{\mathbf{u}}^{n+1}$ into a linear combination form, using the nonlocal variable R^{n+1}, which is expressed as follows:

$$\tilde{\mathbf{u}}_h^{n+1} = \tilde{\mathbf{u}}_{h1}^{n+1} + R^{n+1}\tilde{\mathbf{u}}_{h2}^{n+1}. \tag{3.71}$$

We solve $\tilde{\mathbf{u}}_{h1}^{n+1}$ and $\tilde{\mathbf{u}}_{h2}^{n+1}$ as follows. By substituting $\tilde{\mathbf{u}}_h^{n+1}$ with (3.71) in (3.35), and subsequently dividing the resulting equation based on the nonlocal variable R^{n+1}, we derive the following two sub-equations:

$$\begin{cases} \frac{3}{2\delta t}(\psi_h^{n+1}\tilde{\mathbf{u}}_{h1}^{n+1}, \psi_h^{n+1}\mathbf{v}_h) + \nu(\psi_h^{n+1}\nabla\tilde{\mathbf{u}}_{h1}^{n+1}, \nabla\mathbf{v}_h) + \nu\xi(q(\hat{\phi}_h^{n+1})\tilde{\mathbf{u}}_{h1}^{n+1}, \mathbf{v}_h) \\ \qquad = (\psi_h^{n+1}\frac{4\psi_h^n\mathbf{u}_h^n - \psi_h^{n-1}\mathbf{u}_h^{n-1}}{2\delta t} - \psi_h^{n+1}\nabla P_h^n, \mathbf{v}_h), \\ \frac{3}{2\delta t}(\psi_h^{n+1}\tilde{\mathbf{u}}_{h2}^{n+1}, \psi_h^{n+1}\mathbf{v}_h) + \nu(\psi_h^{n+1}\nabla\tilde{\mathbf{u}}_{h2}^{n+1}, \nabla\mathbf{v}_h) + \nu\xi(q(\hat{\phi}_h^{n+1})\tilde{\mathbf{u}}_{h2}^{n+1}, \mathbf{v}_h) \\ \qquad = (-\psi_h^*(\mathbf{u}_h^* \cdot \nabla)\mathbf{u}_h^*, \mathbf{v}_h). \end{cases} \tag{3.72}$$

Note that all terms, such as ψ_h^{n+1}, $\hat{\phi}_h^{n+1}$, and those on the right side of (3.72), are already obtained from step 1. Therefore, solving $\tilde{\mathbf{u}}_{h1}^{n+1}$ and $\tilde{\mathbf{u}}_{h2}^{n+1}$ becomes straightforward, as it involves solving elliptic equations with variable coefficients. Meanwhile, the variable coefficients within the two equations of (3.72) are positive, a condition ensured by the clamped value $\hat{\phi}_h^{n+1}$ being within $[-1+\varepsilon, 1-\varepsilon]$ and ψ_h^{n+1} falling within $[\frac{\varepsilon}{2}, 1-\frac{\varepsilon}{2}]$. This positivity implies that the solvability of these equations is quite straightforward, facilitated by the application of the Lax-Milgram Theorem.

We continue to solve the nonlocal variable R^{n+1}. By using the splitting form given in (3.71), we formulate (3.36) into the following form:

$$(\frac{3}{2\delta t} - \zeta_2)R^{n+1} = \frac{4R^n - R^{n-1}}{2\delta t} + \zeta_1, \tag{3.73}$$

where

$$\zeta_1 = \left(\psi^*(\mathbf{u}_h^* \cdot \nabla)\mathbf{u}_h^*, \tilde{\mathbf{u}}_{h1}^{n+1}\right), \quad \zeta_2 = \left(\psi^*(\mathbf{u}_h^* \cdot \nabla)\mathbf{u}_h^*, \tilde{\mathbf{u}}_{h2}^{n+1}\right). \tag{3.74}$$

We prove the solvability of (3.73) by showing $\frac{3}{2\delta t} - \zeta_2 \neq 0$. By taking the L^2 inner product of $\tilde{\mathbf{u}}_2^{n+1}$ with the second equation of (3.72), we deduce

$$\begin{aligned} -(\psi_h^*(\mathbf{u}_h^* \cdot \nabla)\mathbf{u}_h^*, \tilde{\mathbf{u}}_{h2}^{n+1}) = \frac{3}{2\delta t}\|\psi_h^{n+1}\tilde{\mathbf{u}}_{2h}^{n+1}\|^2 + \nu\|\sqrt{\psi_h^{n+1}}\nabla\tilde{\mathbf{u}}_{2h}^{n+1}\|^2 \\ + \nu\xi\|\sqrt{q(\hat{\phi}_h^{n+1})}\tilde{\mathbf{u}}_{h2}^{n+1}\|^2 \geq 0, \end{aligned} \tag{3.75}$$

which implies $\frac{3}{2\delta t} - \zeta_2 > 0$. Thus (3.73) is always solvable. Once R^{n+1} is solved, we update $\tilde{\mathbf{u}}_h^{n+1}$ from (3.71).

The implementation of step 3 is straightforward, as it involves solving a pressure Poisson equation with constant coefficients, which can be addressed directly.

In summary, the three steps of the developed algorithm include: the first step, which involves solving four distinct elliptic equations with constant coefficients; the second step, which involves two additional independent elliptic equations; and the third step, which involves a further Poisson equation, also with constant coefficients. The entire implementation process demonstrates that the computation of the developed scheme is linear and fully decoupled.

Remark 3.8. To the best of the authors' knowledge, the only available numerical scheme with decoupling characteristics is the first-order (in time) scheme presented in [39]. The decoupling technique used in [39] is based on the first-order linear stabilizer. To make the scheme clearer, we focus exclusively on the decoupling technique used to separate the computations of ϕ and T, omitting other terms deemed irrelevant to ensure the decoupling approach remains straightforward. The semi-discrete scheme described in [39] is as follows:

$$\begin{cases} \dfrac{\phi^{n+1}-\phi^n}{\delta t} + \cdots\cdots = -\dfrac{\lambda}{\epsilon}p^n\Big(T^n + \underbrace{K\delta t p^n \dfrac{\phi^{n+1}-\phi^n}{\delta t}}_{\text{first-order stabilization term}}\Big), \\ \dfrac{T^{n+1}-T^n}{\delta t} + \cdots\cdots = \underbrace{K p^n \dfrac{\phi^{n+1}-\phi^n}{\delta t}}_{\text{explicit since } \phi^{n+1} \text{ is obtained above}}, \end{cases} \tag{3.76}$$

In the scheme described, a stabilization term of first-order is incorporated into the equation for ϕ^{n+1}, which serves to improve numerical stability and support decoupling. It is shown in [39], that the scheme (3.76) achieves unconditional energy stability. However, the stabilization term introduces variable coefficients of ϕ^{n+1} at each time step, raising the computational complexity and cost. Furthermore, given the particular nature of the stabilization term, the scheme (3.76) is currently limited to a first-order version, and currently, no similar second-order versions exist, presenting considerable difficulties in algorithm development.

In contrast to the above scheme, our developed scheme (3.31)-(3.38) achieves a distinct configuration with second-order temporal accuracy and a completely decoupling structure. These advantages significantly elevate its practical performance, delivering enhanced efficiency and accuracy in computational applications.

4. Numerical simulations

In this section, we conduct numerical tests to verify the convergence rates of the proposed explicit-SAV scheme (3.31)-(3.38) (denoted by ESAV for short). Examples of four-fold and six-fold dendritic growth are performed through extensive 2D and 3D numerical simulations. We employ the Taylor-Hood element [7] for the pair of $(\mathbf{V}_h, O_h)$, which meets the inf-sup condition. This approach utilizes the spaces specified in (3.22), where $l_1 = 1$ and $l_2 = 2$.

4.1. Accuracy test

We perform accuracy tests in 2D to verify the accuracy of the scheme ESAV. The computational domain is set as $\Omega = [0, 2\pi]^2$ with the boundary conditions specified in (2.10). We assume that initial solutions of $\phi, T, \mathbf{u}, P$ read as follows:

$$\begin{aligned} &\phi_0(x,y) = \tanh\Big(\frac{1.5 - \sqrt{(x-\pi)^2 + (y-\pi)^2}}{\epsilon}\Big), \\ &T_0(x,y) = -0.55\phi_0(x,y), \mathbf{u}_0(x,y) = \mathbf{0}, P_0(x,y) = 0. \end{aligned} \tag{4.1}$$

The model parameters are set as

$$\begin{cases} \tau = 1, \lambda = 1, \nu = 1, \xi = 0.01, D = 0.25, \varepsilon = 1\text{e}{-6}, \\ \epsilon = 0.08, K = 1, B = 10, S_1 = 0.5, S_2 = 4. \end{cases} \tag{4.2}$$

We start by verifying the convergence order regarding temporal discretizations. To isolate the impact of temporal discretization on the error, we need to make the error introduced by spatial discretization small enough. Due to the absence of exact solutions, we employ the method of time step refinement to assess errors stemming from temporal discretization. In Fig. 4.1, with the fixed grid

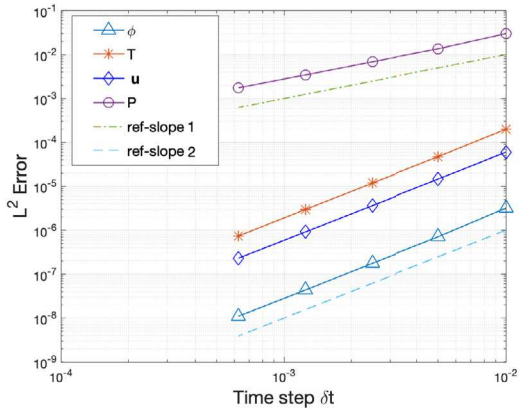

(a) Isotropic case with $\epsilon_4 = 0$.

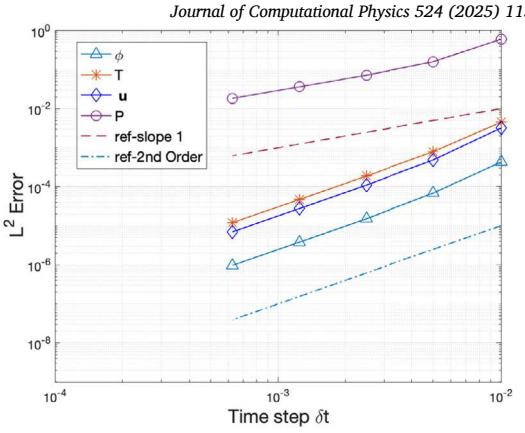

(b) Anisotropic case with $\epsilon_4 = 0.25$.

Fig. 4.1. Accuracy tests for temporal discretization. The L^2-numerical errors of all variables at $t = 1$ for (a) the isotropic case with $\epsilon_4 = 0$, and (b) the anisotropic case with $\epsilon_4 = 0.25$, computed using various δt. The initial conditions are specified in (4.1), and other model parameters are detailed in (4.2).

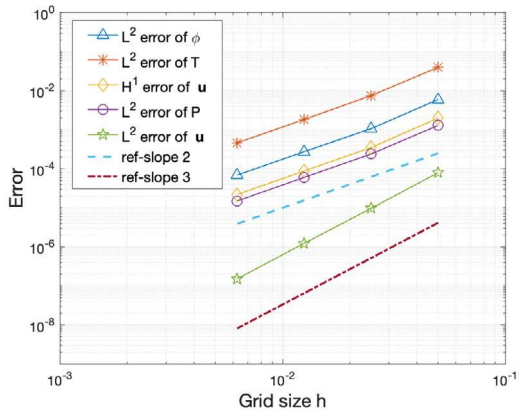

(a) Accuracy tests for spatial discretization.

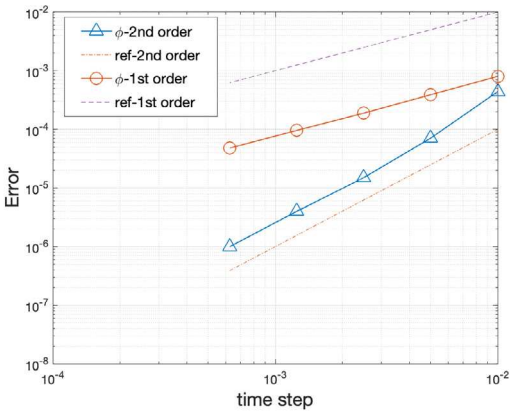

(b) Accuracy comparisons.

Fig. 4.2. (a) Accuracy tests for spatial discretization, where the numerical errors at $t = 1$ in various norms for all variables for the anisotropic case $\epsilon_4 = 0.25$; and (b) accuracy comparison between the developed second-order ESAV scheme and the first-order decoupled scheme developed in [39] for the anisotropic case $\epsilon_4 = 0.25$. The initial conditions are specified in (4.1), and other model parameters are detailed in (4.2).

size of $h = \frac{2\pi}{512}$, we show the L^2-numerical errors for all variables at $t = 1$ both for the isotropic case ($\epsilon_4 = 0$) and the anisotropic case ($\epsilon_4 = 0.25$). The convergence plots reveal that our ESAV scheme achieves a second-order convergence rate for the variables ϕ, T, and $\mathbf{u}$, and a first-order convergence rate for the pressure P.

We continue to assess the convergence order regarding spatial discretizations. Similar to the tests of temporal error, to isolate the impact of spatial discretization on the error, we need to adopt a sufficiently small time step, $\delta t = 1\text{e}{-5}$, to ensure the temporal discretization error remains negligible. Fig. 4.2 depicts the computed numerical errors for different mesh sizes h, specifically in the anisotropic case with $\epsilon_4 = 0.25$. The results indicate that the velocity in the H^1 norm, along with the pressure, phase-field variable, and temperature in the L^2 norm, exhibit a second-order convergence rate for h. The velocity in the L^2 norm shows a third-order convergence rate for h. These obtained convergence rates align with the anticipated theoretical accuracy for $(\mathbf{u}, P)$ using the $P2/P1$ elements, and for ϕ, T using the $P1$ elements.

Using the same example, we illustrate the advantage of the second-order ESAV scheme developed in this article in terms of accuracy by comparing it with the first-order decoupled scheme developed in [39]. It can be observed that when the adopted time step size is relatively large, such as $\delta t = 0.01$, the accuracy difference between the first-order and second-order schemes is not significant, with the error generated by the second-order scheme being slightly smaller than that of the first-order scheme. As the time step size decreases, the error curve of the scheme in [39] follows a first-order convergence rate, whereas the proposed ESAV scheme achieves a second-order convergence rate. For instance, when the time step size is 1.25e−3, the error obtained using the scheme in [39] is 9.6e−5, while the error achieved by the second-order ESAV scheme is only 3.9e−6, which is approximately only 4% of the former. This demonstrates the significant accuracy advantage of the second-order scheme over the first-order scheme in [39]. In addition to accuracy, computational efficiency is a key advantage of the proposed second-order ESAV scheme. While the scheme in [39] is

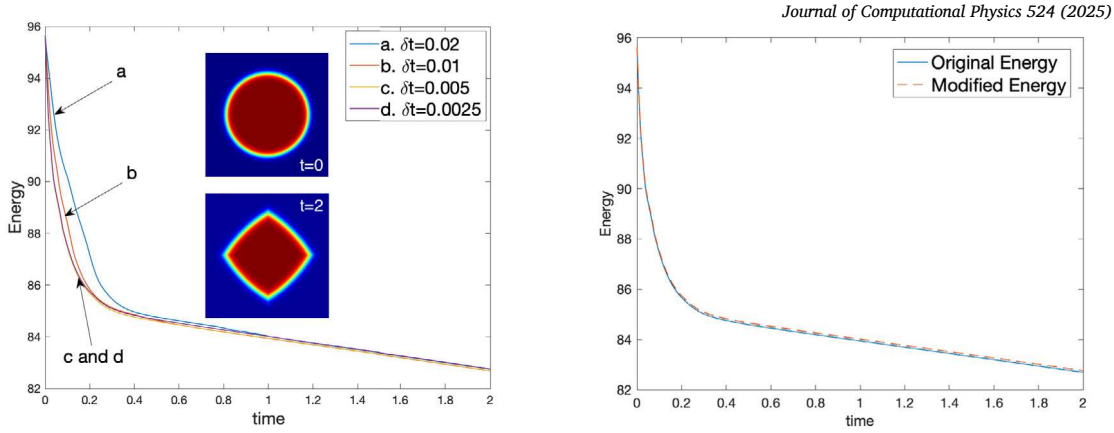

(a) Energy evolution using various time step δt. (b) Original energy and modified energy using $\delta t = 0.01$.

Fig. 4.3. (a) Energy evolution curves computed using various time step δt (snapshots of the profile ϕ at the initial moment and steady state are attached); (b) the original energy (2.13) and the modified energy (3.43) computed with $\delta t = 0.01$. (For interpretation of the colors in the figure(s), the reader is referred to the web version of this article.)

decoupled, it requires solving a variable-coefficient equation for ϕ, which incurs a higher computational cost. In contrast, the current ESAV scheme only requires solving a constant-coefficient elliptic equation for ϕ, resulting in considerable computational savings. For this particular test, with $\delta t = 0.005$, our numerical test indicates that solving the equation for ϕ using the first-order scheme in [39] requires approximately five times more computational time compared to the current ESAV scheme for each time step.

Concerning the stability, we illustrate the temporal evolution of the total free energy, computed by adjusting the time step size, δt. The grid size is set as $h = \frac{2\pi}{512}$. The initial conditions and model parameters used are still specified in (4.1) and (4.2), respectively. We only focus on the anisotropic scenario characterized by $\epsilon_4 = 0.25$. Fig. 4.3(a) presents energy evolution curves obtained using the ESAV scheme, where different time step sizes are employed. The results clearly show that all energy curves demonstrate a consistent downward trend, verifying the scheme's unconditional stability. We also attach the initial and steady-state profiles of ϕ; the final contour forms a rhombus. Fig. 4.3(b) demonstrates the evolution of the total free energy in both its original and modified discrete forms (given in (2.13) and (3.43)) computed with the time step $\delta t = 0.01$, respectively. The observed differences between the energy forms are small, underscoring the negligible discrepancies.

4.2. Anisotropic crystal growth under the flow field

This subsection focuses on simulating the impact of fluid flow on crystal growth. Inspired by Kobayashi's influential study [14], which highlighted the significant effect of the latent heat parameter K on dendrite morphology, we adopt a similar approach by adjusting the parameter K. By introducing a flow field that moves from the top to the bottom boundary, we aim to investigate how fluid dynamics influence the final shape of the dendrites. We will compare the resulting dendrite shapes with those formed in scenarios without a flow field, to clearly illustrate the impact of fluid flow on crystal morphology.

4.2.1. 2D dendritic growth

We begin by implementing 2D simulations. The initial setup positions a tiny circular crystal at the domain's center, with the flow direction established from the top to the bottom boundary. This configuration is specifically designed to systematically investigate the impact of flow field on the growth patterns of the crystal.

The domain is set as $\boldsymbol{x} = (x, y) \in \Omega = [0, L]^2$, with the initial condition, ϕ_0, consisting of a small circular region centered within the domain, that reads as

$$\begin{aligned} &\mathbf{u}_0(\boldsymbol{x}) = \mathbf{0}, p_0(\boldsymbol{x}) = 0, \\ &\phi_0(\boldsymbol{x}) = \tanh\left(\frac{0.05 - |\boldsymbol{x} - \boldsymbol{x}_0|}{0.01}\right), \ T_0(\boldsymbol{x}) = \begin{cases} 0, & \phi_0(\boldsymbol{x}) > 0; \\ -0.55, & \text{otherwise}, \end{cases} \end{aligned} \tag{4.3}$$

with $\boldsymbol{x}_0 = (1, 1)$. We set the model parameters as

$$\begin{cases} L = 2, \lambda = 355, D = 2.25\text{e}{-4}, \tau = D^{-1}, \epsilon = 1.12\text{e}{-2}, \nu = 1, \varepsilon = 1\text{e}{-6}, \\ \xi = 0.01, B = 5 \times 10^4, \epsilon_4 = 0.05, S_1 = 0.9, S_2 = 4, \delta t = 0.01. \end{cases} \tag{4.4}$$

The boundary conditions of ϕ, T, and $\mathbf{u} = (u, v)$ are set as follows,

$$\partial_{\mathbf{n}}\phi|_{\partial\Omega} = 0, \partial_{\mathbf{n}}T|_{\partial\Omega} = 0, u|_{\partial\Omega} = 0, v|_{x=0,L} = 0, v|_{y=0,L} = v_0. \tag{4.5}$$

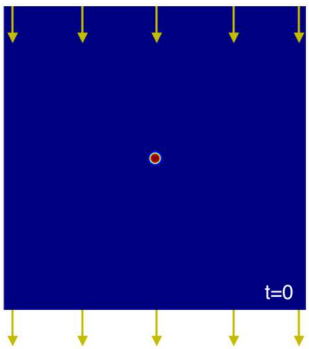

Fig. 4.4. The small 2D crystal nucleus at the initial moment is positioned at the center of the computational domain. In-flow and out-flow conditions are shown at the boundary, with the direction of the flow field indicated by arrows for a better understanding.

We start with the four-fold heterogeneous growth, as specified in (2.8), using a spatial grid size of $h = \frac{2}{512}$. The initial profile of ϕ_0 is depicted in Fig. 4.4, where arrows on the boundary illustrate the flow field direction for a better understanding.

In Fig. 4.5(a), we conduct the no-flow simulations by setting $\mathbf{u}(\boldsymbol{x}, t) = \mathbf{0}$ and varying the latent heat parameter K. The dendritic patterns formed before the long branches reach the domain boundaries are shown, utilizing five different values of $K = 0.55$, 0.6, 0.65, 0.7, 0.8, arranged from left to right. With smaller K values, the branches tend to be thicker. For instance, at $K = 0.5$, the crystal's final shape closely resembles a rhombus. As K increases, the branches gradually become narrower and the tips sharper. Notably, at $K = 0.8$, the crystal develops four very sharp and thin tips.

We further apply a flow field at the domain boundary, setting $v_0 = -0.01$ in (4.5). All other model parameters remain consistent with the no-flow simulations. The effects of the flow on crystal growth are depicted in Fig. 4.5(b), showcasing five different crystal patterns with varying latent heat parameters K. This demonstrates that the crystal growth dynamics under flow conditions diverge markedly from the no-flow scenario. The rate of growth at the upstream tip significantly exceeds that observed at the downstream and horizontal tips. This increased growth rate can be attributed to the upstream tip's direct exposure to the flow field, which reduces the thickness of the thermal boundary layer on this side due to enhanced convective heat transfer. Conversely, the growth rate of the downstream tip is the slowest among the tips due to the expansion of the thermal boundary layer caused by the shielding effect of the crystal itself. The two horizontal tips grow at a rate between that of the upper and lower tips and display a distinctive "tilting" shape, slightly upward. This is a direct consequence of the asymmetrical distribution of heat flux on the upper and lower sides of the horizontal arms, driven by the directional flow field. This phenomenon highlights the complex interplay of heat and mass transfer under the influence of an external flow, leading to anisotropic growth patterns in the crystal structure. It is worth noting that all these numerical results are consistent with findings from studies given in [2,25], highlighting their reliability.

In Fig. 4.5(c), for the case of $K = 0.8$, we plot the velocity profiles $\mathbf{u}$ and $t = 80$. To enhance visibility, the flow field has been mapped onto a grid that is roughly ten times less dense than the computational grid. A small region framed in the first subfigure is enlarged in the second subfigure for a detailed view. Notably, the flow field is confined entirely to the liquid phase outside the dendrite, confirming that there is no flow within the dendrite itself. In Fig. 4.5(d), the profiles for temperature T and pressure P are displayed, and it is evident that the contour of the temperature T aligns cohesively with the dendrite interface depicted by the phase-field variable ϕ.

Next, we investigate the six-fold heterogeneous growth, i.e., $m = 6$ in (2.7), and compare the no-flow and flow-coupled scenarios too. The computation region is defined as $(x, y) \in \Omega = [0, L]^2$ with $L = 2\pi$. Initial conditions for $\phi_0, T_0, \mathbf{u}_0, p_0$ and boundary conditions are consistent with the four-fold simulations, i.e., (4.3) with $\boldsymbol{x}_0 = (\pi, \pi)$ and (4.5). The parameters are the same as (4.4) except that λ is adjusted to $\lambda = 380$ and the spatial grid size h is set as $h = \frac{2\pi}{1024}$. The dendritic patterns in the no-flow scenario are shown in Fig. 4.6(a) using five latent heat parameters: $K = 0.65, 0.7, 0.75, 0.8, 0.85$. When K is small, such as $K = 0.65$, the resulting pattern closely resembles a standard hexagon. As K increases (e.g., $K = 0.7$ and $K = 0.75$), the dendrites evolve into snowflake-like shapes with many fractal-shaped twigs. As K further increases, there is a noticeable decrease in the formation of these small branches (e.g., $K = 0.8$ and $K = 0.85$).

We continue our simulations by applying a flow field (i.e., $v_0 = -0.01$ in (4.5)). Snapshots of the phase-field variable ϕ are presented in Fig. 4.6(b), demonstrating the significant impact of the flow field on the crystal's morphology. This influence mirrors the effects observed in four-fold crystal growth under similar conditions, where the upstream tip exhibits the highest growth rate, while the lower tip grows the slowest. The middle four tips, exhibiting intermediate growth rates, also display a characteristic upward "tilting" shape. In Fig. 4.6 (c) and (d), we show the velocity field, the temperature T, and pressure P for the case of $K = 0.75$ at $t = 195$.

4.2.2. 3D six-fold dendritic growth

We explore the 3D crystallization of dendrites featuring six-fold anisotropy and examine how their structures are influenced by an external flow field. We also provide a comparison between scenarios with no-flow and flow-coupled cases. The computation region is $\boldsymbol{x} = (x, y, z) \in \Omega = [0, L]^3$ with $L = 2\pi$, and the initial conditions are set as

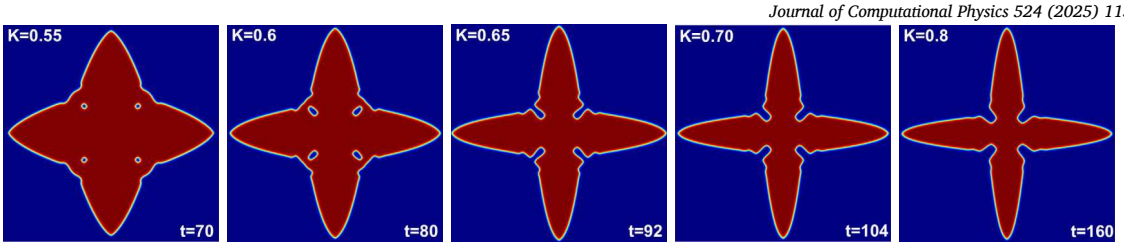

(a) No-flow cases using various K.

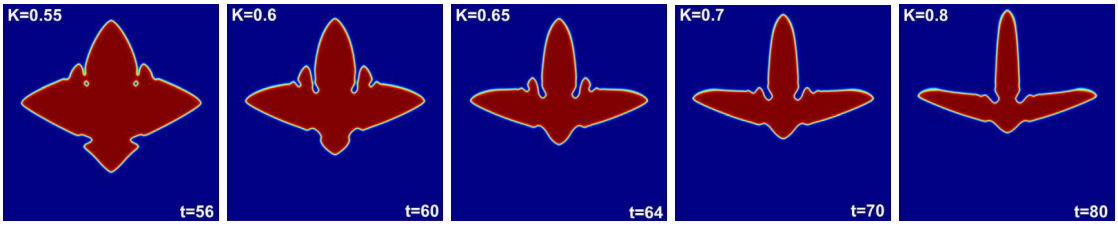

(b) Flow-coupled cases using various K.

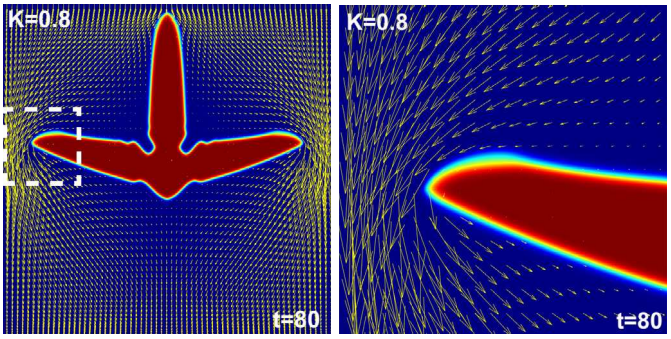

(c) The velocity field $\mathbf{u}$ imposed on the profile ϕ for $K = 0.8$ at $t = 80$.

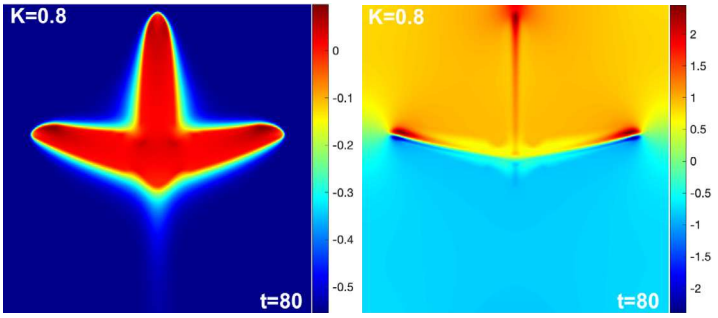

(d) The temperature T and pressure P for $K = 0.8$ at $t = 80$.

Fig. 4.5. 2D four-fold dendritic crystal pattern formed using five distinct latent heat parameters ($K = 0.55, 0.6, 0.65, 0.7, 0.8$ from left to right), where (a) no-flow scenario, (b) flow-coupled scenario, (c) the velocity field superimposed on the profile of ϕ for $K = 0.8$ at $t = 80$ with an enlarged view of the local domain, and (d) temperature and pressure profiles for the same case.

$$\begin{aligned} &\phi_0(\boldsymbol{x}) = \tanh\left(\frac{0.1 - |\boldsymbol{x} - \boldsymbol{x}_0|}{0.02}\right),\ T_0(\boldsymbol{x}) = \begin{cases} 0, & \phi_0(\boldsymbol{x}) > 0; \\ -0.55, & \text{otherwise}, \end{cases} \\ &\mathbf{u}_0(\boldsymbol{x}) = \mathbf{0},\ P_0(\boldsymbol{x}) = 0, \end{aligned} \tag{4.6}$$

with $\boldsymbol{x}_0 = (\pi, \pi, \pi)$. The model parameters are set as

$$\begin{cases} \lambda = 380,\ D = 6.5\text{e}{-3},\ \tau = 500,\ \epsilon = 2\text{e}{-2},\ \nu = 1,\ h = \dfrac{2\pi}{256},\ \varepsilon = 1\text{e}{-6}, \\ \xi = 0.01,\ B = 5 \times 10^4,\ \epsilon_4 = 0.05,\ S_1 = 0.9,\ S_2 = 4,\ \delta t = 0.01. \end{cases} \tag{4.7}$$

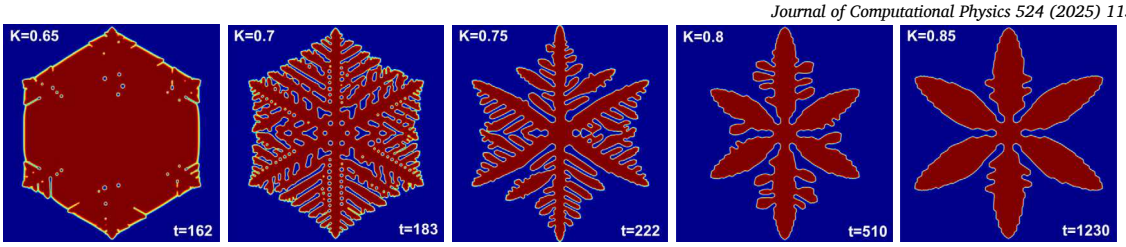

(a) No-flow cases using various K.

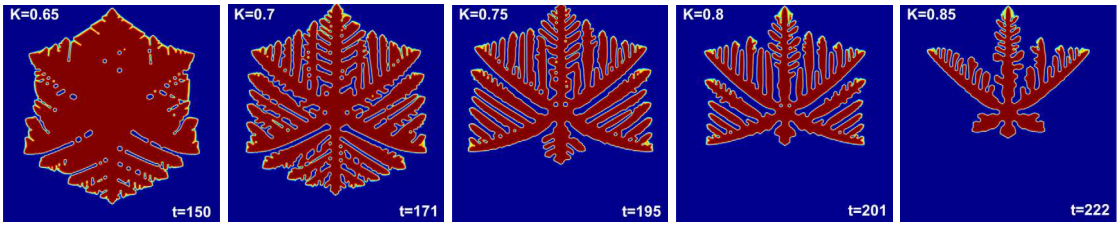

(b) Flow-coupled cases using various K.

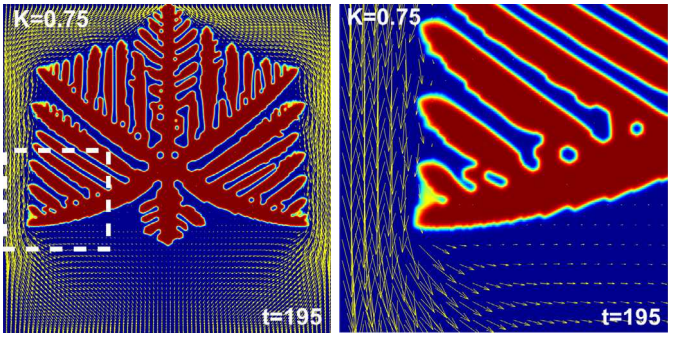

(c) The velocity field imposed on the profile ϕ for $K = 0.8$ at $t = 80$.

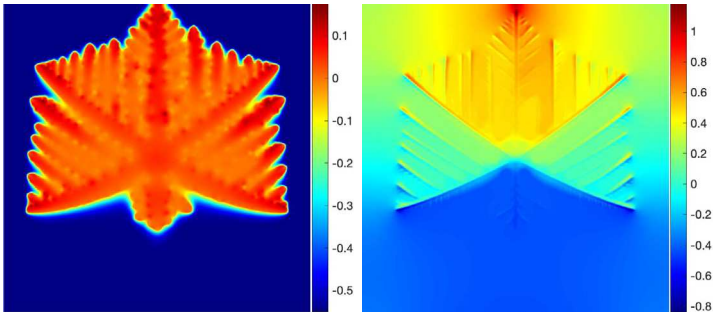

(d) The temperature T and pressure P for $K = 0.8$ at $t = 80$.

Fig. 4.6. 2D six-fold dendritic crystal pattern formed using five distinct latent heat parameters ($K = 0.65, 0.7, 0.75, 0.8, 0.85$ from left to right), where (a) no-flow scenario, (b) flow-coupled scenario, (c) the velocity field superimposed on the profile of ϕ for $K = 0.75$ at $t = 195$ with an enlarged view of the local domain, and (d) temperature and pressure profiles for the same case.

In the z-direction, the boundary conditions for the variables ϕ, T, and $\mathbf{u} = (u, v, w)$ are set as follows,

$$\partial_{\mathbf{n}}\phi|_{z=0,L} = 0, \partial_{\mathbf{n}}T|_{z=0,L} = 0, u|_{z=0,L} = 0, v|_{z=0,L} = 0, w|_{z=0,L} = w_0. \tag{4.8}$$

We first perform simulations for the no-flow case, varying the latent heat parameters to $K = 1$, 1.25, 1.5. Snapshots of the isosurface $\{\phi = 0\}$ before the dendritic branches touch the boundary are shown in Fig. 4.7(a), where the dendrites exhibit a maple-like shape. As K increases, the branches become noticeably thinner. We then couple a flow field by setting $w_0 = -0.01$ in (4.8) and re-conduct simulations. Snapshots of the isosurface $\{\phi = 0\}$ before the fastest-growing tip touches the boundary are shown in Fig. 4.7(b). The flow field significantly alters the crystal structure; similar to the 2D simulation, the branch oriented towards the flow field grows the fastest.

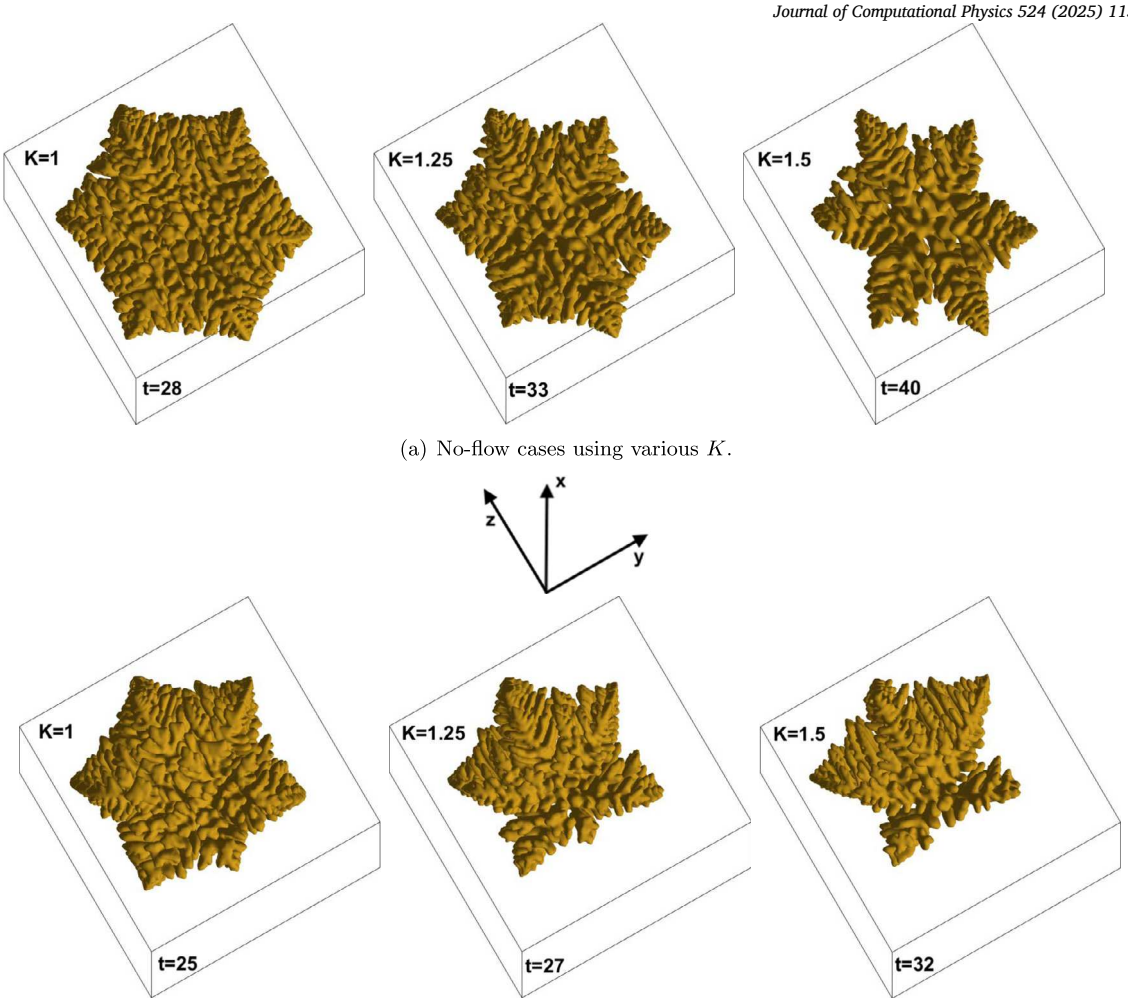

(a) No-flow cases using various K.

(b) Flow-coupled cases using various K.

Fig. 4.7. 3D six-fold dendritic crystal using three different latent heat parameters ($K = 1, 1.25, 1.5$ from left to right), where (a) is no-flow case, and (b) is the flow-coupled case. In each subfigure, the isosurface $\{\phi = 0\}$ is plotted.

5. Concluding remarks

This article designs the first, efficient fully discrete numerical scheme for solving the hydrodynamically coupled phase-field dendritic solidification model. The scheme is anchored on the innovative explicit-SAV method, which is instrumental in the linearization of nonlinear potentials and the establishment of a decoupled structure. This method capitalizes on a distinctive property—"zero-energy contribution"—exhibited by the coupled nonlinear terms. In addition, the approach involves the definition of multiple auxiliary variables, a strategic move that aids in the reformulation of the governing system. This systematic restructuring is pivotal in achieving the desired computational efficiency and accuracy. The scheme's decoupled architecture permits the independent calculation of all variables at every time step, ensuring an operationally efficient framework. The robustness of the approach is also reinforced by its unconditional energy stability and the effectiveness has been demonstrably proven through a series of comprehensive numerical tests conducted in both 2D and 3D, underscoring its applicability and reliability in practical scenarios. To the authors' knowledge, this article's numerical algorithm represents a pioneering achievement—it is the first of the "desired" type fully discrete algorithm for solving this highly nonlinear and coupled phase-field dendritic model.

CRediT authorship contribution statement

Jun Zhang: Writing – original draft, Visualization, Validation. **Kejia Pan:** Writing – original draft, Validation, Methodology. **Xiaofeng Yang:** Writing – review & editing, Writing – original draft, Visualization, Validation, Supervision, Methodology, Investigation, Funding acquisition, Conceptualization.

Declaration of competing interest

The authors declare that they have no known competing financial interests or personal relationships that could have appeared to influence the work reported in this paper.

Acknowledgements

The work of J. Zhang was partially supported by the Scientific Research Foundation of Guizhou University of Finance and Economics (Grant No. 2024XSXMA10). The work of X. Yang was partially supported by National Science Foundation with grant number DMS-2309731. We are grateful for resources from the High Performance Computing Center of Central South University. J. Zhang and K. Pan contributed equally to this work and should be considered co-first authors.

Data availability

No data was used for the research described in the article.

References

[1] H. Abels, H. Garcke, G. Grün, Thermodynamically consistent, frame indifferent diffuse interface models for incompressible two-phase flows with different densities, Math. Models Methods Appl. Sci. 22 (2012).
[2] C. Beckermann, H.-J. Diepers, I. Steinbach, A. Karma, X. Tong, Modeling melt convection in phase-field simulations of solidification, J. Comput. Phys. 154 (1999) 468–496.
[3] E. Bänsch, Finite element discretization of the Navier–Stokes equations with a free capillary surface, Numer. Math. 88 (2001) 203–235.
[4] C. Chen, X. Yang, Efficient numerical scheme for a dendritic solidification phase field model with melt convection, J. Comput. Phys. 388 (2019) 41–62.
[5] C. Chen, X. Yang, Efficient fully-decoupled and fully-discrete Explicit-IEQ numerical algorithm for the two-phase incompressible flow-coupled Cahn-Hilliard phase-field model, Sci. China Math. 67 (2024) 2171–2194.
[6] W. E, J.G. Liu, Projection method. I. Convergence and numerical boundary layers, SIAM J. Numer. 32 (1995) 1017–1057.
[7] V. Girault, P.A. Raviart, Finite Element Method for Navier-Stokes Equations: Theory and Algorithms, Springer-Verlag, Berlin, Heidelberg, 1987, pp. 395–414.
[8] J.L. Guermond, L. Quartapelle, A projection fem for variable density incompressible flows, J. Comput. Phys. 165 (4) (2000) 167–188.
[9] J.L. Guermond, A. Salgado, A splitting method for incompressible flows with variable density based on a pressure Poisson equation, J. Comput. Phys. 228 (2009) 2834–2846.
[10] J.-H. Jeong, J.A. Dantzig, N. Goldenfeld, Dendritic growth with fluid flow in pure materials, Metall. Mater. Trans. A 34 (2003) 459–466.
[11] J.-H. Jeong, N. Goldenfeld, J.A. Dantzig, Phase field model for three-dimensional dendritic growth with fluid flow, Phys. Rev. E 55 (2001) 041602.
[12] A. Karma, W. Rappel, Quantitative phase-field modeling of dendritic growth in two and three dimensions, Phys. Rev. E 57 (1998) 4323–4349.
[13] A. Karma, W. Rappel, Phase-field model of dendritic sidebranching with thermal noise, Phys. Rev. E 60 (1999) 3614–3625.
[14] R. Kobayashi, Modeling and numerical simulations of dendritic crystal growth, Physica D 63 (1993) 410.
[15] Q. Li, C. Beckermann, Modeling of free dendritic growth succionitrile-acetone alloys with thermosolutal melt convection, J. Cryst. Growth 236 (2002) 482–498.
[16] H. Neumann-Heyme, K. Eckert, S. Odenbach, Free dendrite growth under modulated flow in pure substances: two-dimensional phase-field simulations, IOP Conf. Ser., Mater. Sci. Eng. 27 (2012) 012045.
[17] Q. Pan, Y. Huang, C. Chen, X. Yang, Y.J. Zhang, The subdivision-based IGA-EIEQ numerical scheme for the Cahn-Hilliard-Darcy system of two-phase Hele-Shaw flow on complex curved surfaces, Comput. Methods Appl. Mech. Eng. 420 (2023) 116709.
[18] Q. Pan, Y. Huang, T. Rabczuk, X. Yang, The subdivision-based IGA-EIEQ numerical scheme for the Navier-Stokes equations coupled with Cahn-Hilliard phase-field model of two-phase incompressible flow on complex curved surfaces, Comput. Methods Appl. Mech. Eng. 424 (2024) 116901.
[19] J. Shen, On error estimates of the projection methods for the Navier-Stokes equations: second-order schemes, Math. Comput. 65 (215) (1996) 1039–1065.
[20] J. Shen, J. Xu, J. Yang, The scalar auxiliary variable (sav) approach for gradient flows, J. Comput. Phys. 353 (2018) 407–416.
[21] J. Shen, J. Xu, J. Yang, A new class of efficient and robust energy stable schemes for gradient flows, SIAM Rev. 404 (2020) 109115.
[22] J. Shen, X. Yang, Decoupled energy stable schemes for phase field models of two phase complex fluids, SIAM J. Sci. Comput. 36 (2014) B122–B145.
[23] J. Shen, X. Yang, Decoupled, energy stable schemes for phase-field models of two-phase incompressible flows, SIAM J. Numer. Anal. 53 (1) (2015) 279–296.
[24] J. Shen, X. Yang, The IEQ and SAV approaches and their extensions for a class of highly nonlinear gradient flow systems, Contemp. Math. 754 (2020) 217–245.
[25] X. Tong, C. Beckermann, A. Karma, Q. Li, Phase-field simulations of dendritic crystal growth in a forced flow, Phys. Rev. E 63 (2001) 061601.
[26] J.A. Warren, W.J. Boettinger, Prediction of dentric growth and microsegregation patterns in a binary alloy using the phase field method, Acta Metall. Mater. 43 (1995) 689–703.
[27] X. Yang, Linear, first and second order and unconditionally energy stable numerical schemes for the phase field model of homopolymer blends, J. Comput. Phys. 327 (2016) 294–316.
[28] X. Yang, Efficient linear, stabilized, second order time marching schemes for an anisotropic phase field dendritic crystal growth model, Comput. Methods Appl. Mech. Eng. 347 (2019) 316–339.
[29] X. Yang, A new efficient fully-decoupled and second-order time-accurate scheme for Cahn-Hilliard phase-field model of three-phase incompressible flow, Comput. Methods Appl. Mech. Eng. 376 (2021) 13589.
[30] X. Yang, A novel fully-decoupled scheme with second-order time accuracy and unconditional energy stability for the Navier-Stokes equations coupled with mass-conserved Allen-Cahn phase-field model of two-phase incompressible flow, Int. J. Numer. Methods Eng. 122 (2021) 1283–1306.
[31] X. Yang, A novel fully-decoupled, second-order and energy stable numerical scheme of the conserved Allen-Cahn type flow-coupled binary surfactant model, Comput. Methods Appl. Mech. Eng. 373 (2021) 113502.
[32] X. Yang, On a novel fully-decoupled, second-order accurate energy stable numerical scheme for a binary fluid-surfactant phase-field model, SIAM J. Sci. Comput. 43 (2021) B479–B507.
[33] X. Yang, A novel fully-decoupled, second-order time-accurate, unconditionally energy stable scheme for a flow-coupled volume-conserved phase-field elastic bending energy model, J. Comput. Phys. 432 (2021) 110015.
[34] X. Yang, Fully-discrete spectral-Galerkin scheme with decoupled structure and second-order time accuracy for the anisotropic phase-field dendritic crystal growth model, Int. J. Heat Mass Transf. 180 (2021) 121750.
[35] X. Yang, On a novel full decoupling, linear, second-order accurate, and unconditionally energy stable numerical scheme for the anisotropic phase-field dendritic crystal growth model, Int. J. Numer. Methods Eng. 122 (2021) 4129–4153.

[36] X. Yang, M.G. Forest, H. Li, C. Liu, J. Shen, Q. Wang, F. Chen, Modeling and simulations of drop pinch-off from liquid crystal filaments and the leaky liquid crystal faucet immersed in viscous fluids, J. Comput. Phys. 236 (2013) 1–14.
[37] P. Yue, J.J. Feng, C. Liu, J. Shen, A diffuse-interface method for simulating two-phase flows of complex fluids, J. Fluid Mech. 515 (2004) 293–317.
[38] J. Zhang, C. Chen, X. Yang, A novel decoupled and stable scheme for an anisotropic phase-field dendritic crystal growth model, Appl. Math. Lett. 95 (2019) 122–129.
[39] J. Zhang, X. Yang, A fully decoupled, linear and unconditionally energy stable numerical scheme for a melt-convective phase-field dendritic solidification model, Comput. Methods Appl. Mech. Eng. 363 (2020) 112779.
[40] M-F. Zhu, T. Dai, S-Y. Lee, C.-P. Hong, Modeling of solutal dendritic growth with melt convection, Comput. Math. Appl. 55 (2008) 1620–1628.